J. Fluid Mech. (1997), *vol.* 344, *pp.* 95–136. Printed in the United Kingdom

A direct numerical simulation study of flow past a freely vibrating cable

By DAVID J. NEWMAN AND GEORGE EM KARNIADAKIS†

Center for Fluid Mechanics, Division of Applied Mathematics, Brown University, Providence, RI 02912, USA

(Received 26 August 1996 and in revised form 13 January 1997)

We present simulation results of flow-induced vibrations of an infinitely long flexible cable at Reynolds numbers $Re = 100$ and $Re = 200$, corresponding to laminar and early transitional flow states, respectively. The question as to what cable motions and flow patterns prevail is investigated in detail. Both standing wave and travelling wave responses are realized but in general the travelling wave is the preferred response. A standing wave cable response produces an interwoven pattern of vorticity, while a travelling wave cable response produces oblique vortex shedding. A sheared inflow produces a mixed standing wave/travelling wave cable response and chevron-like patterns with vortex dislocations in the wake. The lift force on the cable as well as its motion amplitudes are larger for the standing wave response. At $Re = 200$, the cable and wake response are no longer periodic, and the maximum amplitude of the cable is about one cylinder diameter, in agreement with experimental results.

1. Introduction

One of the major reasons for failure of cables in the ocean is flow-induced vibrations, commonly known as strumming, e.g. see Griffin *et al.* (1982). The design of mooring cables, petroleum production risers, pipelines, and remotely operated vehicle tethers depend critically on the magnitude and frequency of these vibrations. In air flow, similar cylindrical structures are also subject to excitation due to vortex shedding. The failure of the Tacoma Narrows suspension bridge in 1940 is a well-known example of the destructive potential of flow-induced vibrations.

Vortex-induced vibration of a cable is a fluid-elastic problem. The vibration of the cable is driven by the force fluctuations due to vortex shedding, and the vortex shedding is influenced by the motion of the cable (see Blevins 1977; Naudascher & Rockwell 1993). Although separate progress has been made in the modelling of wake flows and predicting cable dynamics (see the reviews by Triantafyllou, Gopalkrishnan & Grosenbaugh 1994; Sarpkaya 1979; Bearman 1984 and Parkinson 1989), understanding the *coupling* of cable and wake dynamics remains unresolved. The fundamental assumption in modelling flow structure interactions is the separation of hydrodynamic loading into vortex flow forces and potential flow forces as first suggested by Taylor (1928) and revisited by Lighthill (1986). However, this classical approach needs to be reconsidered in order to explain the full fluid/structure interaction. The recent progress made in understanding and modelling the near-wake

† Author to whom correspondence should be addressed.

dynamics of bluff bodies offers an opportunity to revisit the vortex-induced vibration problem and provide new predictive models that give an accurate description of the flow field.

Experimental studies of vortex-induced vibrations of flexibly mounted *rigid* cylinders have established two basic facts (see Griffin, Skop & Koopman 1973; Griffin & Koopmann 1977; Staubli 1983; Griffin 1992). First, vortex-induced vibration is a self-limiting process, with an upper bound for the vibration amplitude of approximately one cylinder diameter. Second, the magnitude of the lift force weakly depends on the vibration amplitude. However, the phase of the lift force relative to the cylinder motion strongly depends on the vibration amplitude and is the dominant mechanism that limits the vibration amplitude.

For *flexible* cylinders, or vibrating cables, we have the additional complexity of variation of wake properties such as Strouhal number, vortex spacing, and formation length, along the span of the cable (see Ramberg & Griffin 1976). The phase difference between the lift force and cable motion varies along the cable span, and depends on the mass ratio, shear ratio, and Reynolds number. For a standing wave vibration response this phase difference is typically greater at the nodes than at the anti-nodes. For longer wavelength cable vibration where a travelling wave vibration response prevails, the phase difference is constant along the cable span. Therefore, the key issue in hydroelastic problems is predicting the variation of the amplitude and phase of the hydrodynamic forces along a vibrating cable as a function of the motion of the cable. If the hydrodynamic forces are modelled correctly, the existing state-of-the-art cable dynamics computer programs (see Triantafyllou 1994 and Hover, Grosenbaugh & Triantafyllou 1994) can simulate the response of the cable with acceptable accuracy.

Non-dimensional parameters that influence the motion of flexible cables have been analysed by Vandiver (1991) using data from 20 years of field experiments. It was concluded that the parameters which significantly affect the cable response are: the number of resonant natural modes within the shear excitation bandwidth, shear fraction, reduced damping, mass ratio, and turbulence intensity. Predicting the cable response is complicated – in particular the conditions under which 'lock-in' occurs, where the cable vibration locks in to a single frequency and wavelength. The conditions that lead to a multi-modal response are even less well understood and the question of whether lock-in is possible for very long cables has not yet been answered. It is not known if high vibration modes can lock-in, although this has occasionally been observed in field experiments.

At lock-in, the response of marine cables and other marine structures seems to follow a universal curve indicated by the data in figure 1 which includes experimental data from several investigations, compiled by Griffin (1992). The figure plots crossflow vibration amplitude versus the so-called mass-damping or response parameter S_G. The latter is a dimensionless group which is derived based on a normal mode analysis of the equation of motion at lock-in. It is defined as

$$S_G = 8\pi^2 St^2 \zeta_s \frac{\rho}{\rho_f d^2}, \tag{1.1}$$

where $St = fd/U$ is the Strouhal number (with f the shedding frequency, d the cable diameter, and U the free-stream velocity). Also, ζ_s denotes damping due to structural dissipation, and the last term is the mass ratio where ρ is the mass per unit length of the cable and ρ_f is the fluid density. Marine cables typically have a mass-damping (response) parameter less than 1, and the mass ratio in water varies from slightly above 1 to 10. In addition to cables, the data in figure 1 include cantilevers, spring-

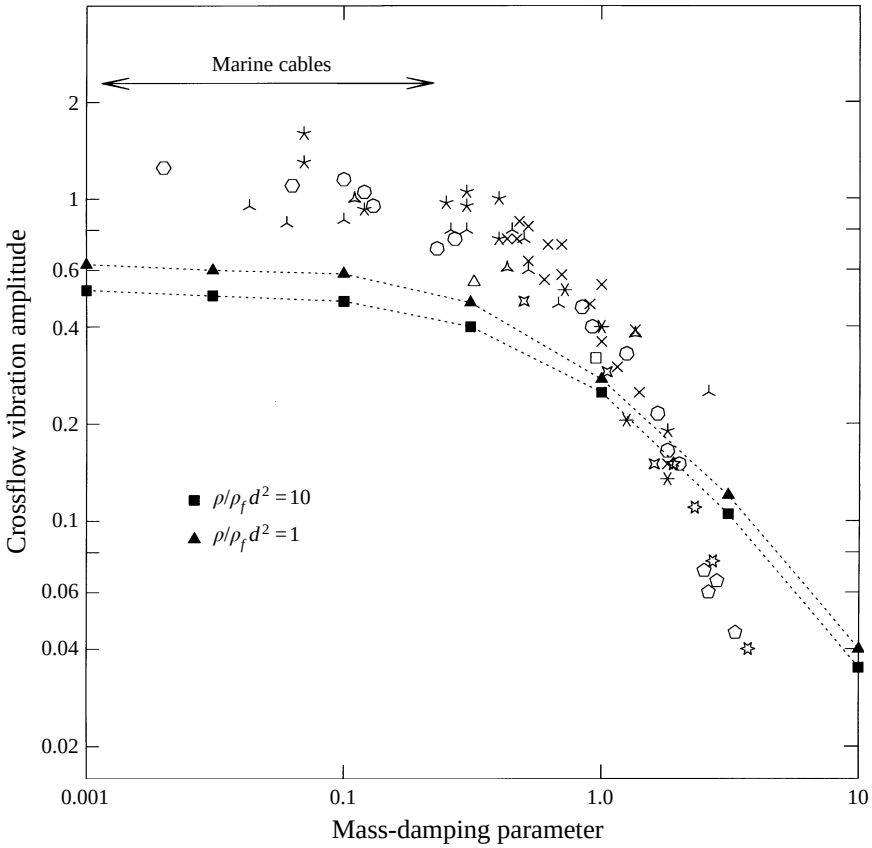

FIGURE 1. Flow-induced crossflow vibration amplitude versus mass-damping (response) parameter. The curve shows our $Re = 100$ two-dimensional simulation results, while the symbols show experimental data compiled by Griffin (1992).

mounted cylinders and pivoted cylinders. A correction factor based on a normal mode analysis has been used to correct for differences in the mode shapes.

The figure also shows our $Re = 100$ *two-dimensional* simulation results of a freely vibrating rigid cylinder for two different mass ratios, first reported in Newman & Karniadakis (1995). The simulation results show the amplitude limiting response as the mass-damping (response) parameter tends to zero, and the attenuation of the vibration amplitude as the mass-damping increases. The simulations underpredict the cylinder vibration amplitude for low values of mass-damping and overpredict the cylinder vibration amplitude for high values of mass-damping. This discrepancy may be explained by the fact that three-dimensionality plays a dominant role in addition to the particular form of cable lock-in motion. The simulations also reveal a monotonic trend with respect to the mass ratio, with lower mass ratio giving a larger amplitude response. This has also been found in experiments and has led to the conclusion that low-mass-ratio cylinders have broader lock-in bandwidth than high-mass-ratio cylinders. The justification for coalescence of mass ratio and damping ratios into a single parameter, i.e. the mass-damping or response parameter, is based on the assumption of simple harmonic motion. At lower values of the mass ratio $\rho/\rho_f d^2$, higher harmonics are introduced and therefore it is less valid to assume that the vibration amplitude depends on just one single combined parameter. Moreover,

within the lock-in regime there is some variation in the response amplitude as discussed in §3. An additional explanation for the discrepancy is Reynolds number effects, since the experiments correspond to a range $300 < Re < 10^6$ while the simulation results in figure 1 are for $Re = 100$. Two-dimensional simulations at $Re = 200$ by Blackburn & Karniadakis (1993) have produced similar trends to our $Re = 100$ simulations.

Current models of cable motion couple the displacement equation with the flow using the cross-sectional force coefficient. This force coefficient is modelled either using a series of approximations fitted with experimental data or by using a nonlinear van der Pol type equation, as in the work of Hartlen & Curie (1970). Parkinson (1989) remarks that there is skepticism about these models, particularly in the light of their failure to even qualitatively predict experimentally observed responses, for example the oscillation hysteresis reported by Brika & Laneville (1993). Simplified models developed by Vandiver & Chung (1987) ignore the details of the flow and their success is based on accurately modelling the added mass coefficient. This added-mass coefficient significantly varies along the cable, and it may even obtain negative values for low-mass-ratio cables, as reported by Chung (1989) and Sarpkaya (1977).

The objective of the present study is to directly simulate the flow past a freely vibrating flexible cable from first principles, i.e. using the full Navier–Stokes equations coupled with the equation of motion for the cable. In this paper, we consider inextensible cables with negligible bending stiffness and negligible internal damping. We simulate flow fields in the laminar ($Re = 100$) and early transitional ($Re = 200$) regimes. We also neglect the effect of different types of cable support by assuming an infinitely long cable and periodicity in the spanwise direction. We specifically focus on the flow patterns and corresponding hydrodynamic loading produced by a cable undergoing a standing wave or a travelling wave flow-induced vibration motion. Several simulations are presented to determine the preferred asymptotic response mode corresponding to different initial states. In nearly all of the simulations the incoming flow is uniform, but in one case we examine the effects of a sheared inflow in which a non-lock-in response is produced.

The paper is organized as follows. In §2 the formulation and numerical method are explained. In §3, the nonlinear response of the coupled system is analysed using two-dimensional simulations. In §4 we consider standing and travelling wave vibration responses at $Re = 100$, and in §5 we investigate the effects of sheared inflow. Section 6 covers transitional wakes at $Re = 200$, and finally the results are summarized and discussed in §7.

2. Formulation

2.1. *Coordinate transformation*

We consider the interaction of an incompressible fluid flowing past a long flexible cable under tension. The equations that describe this problem are the coupled system of fluid equations and cable equations. The Navier–Stokes equations and the continuity equation are the equations of motion of the fluid. In an inertial coordinate system (x', y', z') these are

$$\frac{\partial \boldsymbol{u}'}{\partial t} + (\boldsymbol{u}' \cdot \nabla')\,\boldsymbol{u}' = -\frac{1}{\rho_f}\nabla' p' + \frac{1}{Re}\nabla'^2 \boldsymbol{u}', \tag{2.1}$$

$$\nabla' \cdot \boldsymbol{u}' = 0, \tag{2.2}$$

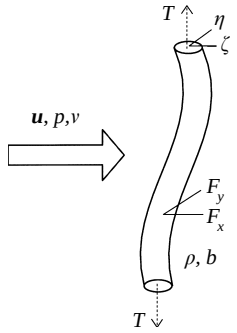

FIGURE 2. Schematic of cable and fluid showing motion and force variables and parameters.

where $\boldsymbol{u}'$ is the velocity field, p' is the pressure, $Re = Ud/v$ is the Reynolds number based on the free-stream velocity U, cable diameter d and kinematic viscosity v, ρ_f is the fluid density, and ∇' is the gradient operator in the inertial coordinate system. By assuming small displacements, the equation of motion of the cable for its two directions of motion is given by the forced vibrating string equation with damping

$$\rho \frac{\partial^2 \boldsymbol{\zeta}}{\partial t^2} + b \frac{\partial \boldsymbol{\zeta}}{\partial t} = T \frac{\partial^2 \boldsymbol{\zeta}}{\partial z^2} + \boldsymbol{F}(z,t), \tag{2.3}$$

where $\boldsymbol{\zeta}(z,t) = (\zeta(z,t), \eta(z,t))$ gives the cable displacement in the streamwise and crossflow directions. The cable has mass per unit length ρ, tension T and damping coefficient b, while $\boldsymbol{F}(z,t)$ is the force on the cable imparted by the fluid. The phase speed of waves in the cable is $c = (T/\rho)^{1/2}$. The force components in the streamwise and crossflow directions are referred to as the drag and lift forces on the cable. We assume that the cable is inextensible and its bending stiffness EI is negligible. Vandiver & Li (1994) suggested that the latter assumption is valid in tension-dominated cases for which $T/EIm^2 > 30$, where m is the wavenumber of the excited mode. In all our cable simulations we assume zero damping ($b = 0$) since this will produce the maximum vibration amplitude (see figure 1). While our focus is on solving the flow-induced vibration problem with the simplest possible cable model, we point out that more complete models of cable dynamics have been derived by Carrier (1945), Irvine & Caughey (1974), Triantafyllou (1985), and Triantafyllou & Howell (1992).

Lift and drag forces are computed along the span of the cable by computing the integral of the pressure and viscous stress terms

$$\boldsymbol{F}(z,t) = \oint \left(-p\boldsymbol{n} + v(\nabla \boldsymbol{u} + \nabla \boldsymbol{u}^T) \cdot \boldsymbol{n}\right) \mathrm{d}s, \tag{2.4}$$

where the integration is performed around the circumference of the cable at each spanwise location and $\boldsymbol{n}$ is the outward unit normal on the cable. A schematic of the fluid/cable system showing the variables and parameters is shown in figure 2.

Solving fluid/structure interaction problems generally involves moving computational domains and dynamic re-meshing. A general method to deal with this moving mesh is by using the Arbitrary Lagrangian Eulerian (ALE) formulation in conjunction with the new spectral discretizations on unstructured grids, Warburton & Karniadakis (1996). However, in our moving cable problem, we can eliminate the difficulty of a moving mesh by attaching the coordinate axes to the cable, i.e. using body-fitted coordinates. This transformation was used by Dimas & Triantafyllou (1994) in stud-

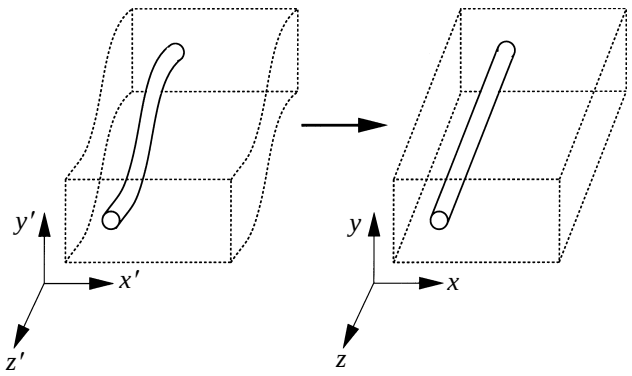

FIGURE 3. The computational domain is mapped from an inertial coordinate system (x', y', z') where the domain boundaries are deformed and moving to a non-inertial coordinate system (x, y, z) where the domain boundaries are non-deformed and stationary.

ies of inviscid free-surface flows. The transformation maps the time-dependent and deforming domain to a stationary and non-deforming one as shown in figure 3. This mapping is described by the following transformation:

$$x = x' - \zeta(z,t), \quad y = y' - \eta(z,t). \tag{2.5a,b}$$

Accordingly, the velocity components and pressure are transformed as follows:

$$u = u' - \frac{\partial \zeta}{\partial t} - w'\frac{\partial \zeta}{\partial z}, \quad v = v' - \frac{\partial \eta}{\partial t} - w'\frac{\partial \eta}{\partial z}, \tag{2.6a,b}$$

$$w = w', \quad p = p'. \tag{2.6c,d}$$

In the transformed system of coordinates the cable appears as straight and stationary. The Navier–Stokes equation (2.1) and continuity equation (2.2) are transformed as follows:

$$\frac{\partial \boldsymbol{u}}{\partial t} + (\boldsymbol{u}\cdot\nabla)\boldsymbol{u} = -\nabla p + \frac{1}{Re}\nabla^2\boldsymbol{u} + \boldsymbol{A}(\boldsymbol{u}, p, \boldsymbol{\zeta}), \tag{2.7}$$

$$\nabla\cdot\boldsymbol{u} = 0, \tag{2.8}$$

where we have redefined the pressure as $p = p'/\rho_f$. The forcing term $\boldsymbol{A}(\boldsymbol{u}, p, \boldsymbol{\zeta})$ is the additional acceleration introduced by the non-inertial transformation (2.1). The x-, y- and z-components of $\boldsymbol{A}$ have components due to inviscid and viscous contributions and are given by

$$A_x = -\frac{\mathrm{d}^2\zeta}{\mathrm{d}t^2} + \frac{1}{Re}\left[\frac{\partial^2}{\partial z'^2}\left(u + \frac{\partial \zeta}{\partial z}w\right) - \frac{\partial^2 u}{\partial z^2} + \frac{\partial \zeta}{\partial z}\nabla^2_{xy}w + \frac{\partial^3 \zeta}{\partial t \partial z^2}\right], \tag{2.9a}$$

$$A_y = -\frac{d^2\eta}{dt^2} + \frac{1}{Re}\left[\frac{\partial^2}{\partial z'^2}\left(v + \frac{\partial \eta}{\partial z}w\right) - \frac{\partial^2 v}{\partial z^2} + \frac{\partial \eta}{\partial z}\nabla^2_{xy}w + \frac{\partial^3 \eta}{\partial t \partial z^2}\right], \tag{2.9b}$$

$$A_z = \frac{\partial \zeta}{\partial z}\frac{\partial p}{\partial x} + \frac{\partial \eta}{\partial z}\frac{\partial p}{\partial y} + \frac{1}{Re}\left[\frac{\partial^2 w}{\partial z'^2} - \frac{\partial^2 w}{\partial z^2}\right], \tag{2.9c}$$

where we define

$$\frac{\mathrm{d}}{\mathrm{d}t} \equiv \frac{\partial}{\partial t} + u\frac{\partial}{\partial x} + v\frac{\partial}{\partial y} + w\frac{\partial}{\partial z}, \tag{2.10a}$$

$$\frac{\partial}{\partial z'} \equiv \frac{\partial}{\partial z} - \frac{\partial \zeta}{\partial z}\frac{\partial}{\partial x} - \frac{\partial \eta}{\partial z}\frac{\partial}{\partial y}, \tag{2.10b}$$

$$\nabla_{xy}^2 \equiv \frac{\partial^2}{\partial x^2} + \frac{\partial^2}{\partial y^2}. \tag{2.10c}$$

We solve the coupled fluid/cable problem in three steps. First, the fluid equations (2.7) are solved given the cable motion $\boldsymbol{\zeta}(z,t)$. Next, the lift and drag forces on the cable are computed as a function of z using (2.4). Finally, the cable motion is updated using (2.3).

2.2. *Numerical method*

The flow and cable variables are assumed to be periodic in the spanwise direction with a periodic length L. This assumption allows us to use a Fourier expansion in the z-direction. The flow and cable motion variables are expanded as

$$\left\{ \begin{array}{c} u(x,y,z,t) \\ v(x,y,z,t) \\ w(x,y,z,t) \\ p(x,y,z,t) \end{array} \right\} = \sum_{m=0}^{M-1} \left\{ \begin{array}{c} u_m(x,y,t) \\ v_m(x,y,t) \\ w_m(x,y,t) \\ p_m(x,y,t) \end{array} \right\} \mathrm{e}^{\mathrm{i}\beta m z}, \tag{2.11}$$

$$\left\{ \begin{array}{c} \zeta(z,t) \\ \eta(z,t) \end{array} \right\} = \sum_{m=0}^{M-1} \left\{ \begin{array}{c} \zeta_m(t) \\ \eta_m(t) \end{array} \right\} \mathrm{e}^{\mathrm{i}\beta m z}, \tag{2.12}$$

where $\beta = 2\pi/L$ is the spanwise wavenumber and M is the number of Fourier modes used in the expansion. The modified Navier–Stokes equations (2.7) and continuity equation (2.8) in the boundary-fitted coordinate system become a system of M two-dimensional partial differential equations coupled by the nonlinear terms

$$\frac{\partial \boldsymbol{u}_m}{\partial t} + [(\boldsymbol{u}\cdot\nabla)\boldsymbol{u}]_m = -\tilde{\nabla} p_m + \frac{1}{Re}\left[\nabla_{xy}^2 - \beta^2 m^2\right]\boldsymbol{u}_m + [\boldsymbol{A}]_m, \tag{2.13}$$

$$\tilde{\nabla}\cdot\boldsymbol{u}_m = 0 \tag{2.14}$$

where $\tilde{\nabla} \equiv (\partial/\partial x, \partial/\partial y, \mathrm{i}\beta m)$. Similarly, the cable equations become a set of M uncoupled ordinary differential equations for each mode m

$$\rho\,\ddot{\boldsymbol{\zeta}}_m + b\,\dot{\boldsymbol{\zeta}}_m + \beta^2 m^2 T\,\boldsymbol{\zeta}_m = \boldsymbol{F}_m(t). \tag{2.15}$$

The equations of motion for the fluid are discretized in time using the high-order fractional-step scheme proposed by Karniadakis, Israeli & Orszag (1991). The first stage of each time step adds all the nonlinear contributions to the velocity field. The nonlinear terms $(\boldsymbol{u}\cdot\nabla)\boldsymbol{u}$ and $\boldsymbol{A}(\boldsymbol{u},p,\boldsymbol{\zeta})$ are computed explicitly using a stiffly stable integration scheme of order J

$$\frac{\hat{\boldsymbol{u}}_m - \sum_{q=0}^{J-1} \alpha_q \boldsymbol{u}_m^{n-q}}{\Delta t} = \sum_{q=0}^{J-1} \beta_q \left[-(\boldsymbol{u}\cdot\nabla)\boldsymbol{u} + \boldsymbol{A}\right]_m^{n-q}, \tag{2.16}$$

where α_q and β_q are the coefficients for stiffly stable integration. We use second-order-accurate time stepping ($J = 2$). The next stage adds the contribution of the pressure gradient to the velocity field and enforces the continuity constraint,

$$\frac{\hat{\hat{\boldsymbol{u}}}_m - \hat{\boldsymbol{u}}_m}{\Delta t} = -\tilde{\nabla} p_m, \qquad \tilde{\nabla}\cdot\hat{\hat{\boldsymbol{u}}}_m = 0, \tag{2.17}$$

along with a consistent Neumann boundary condition for the pressure derived from

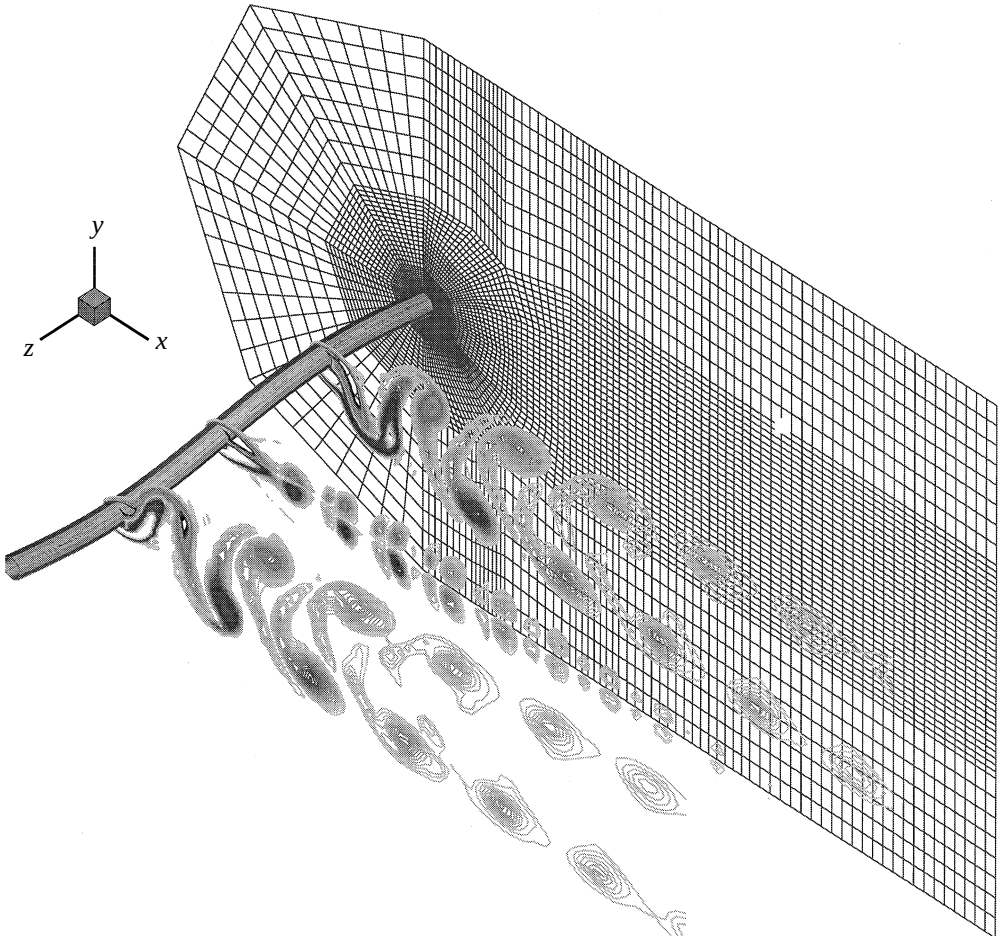

FIGURE 4. A view of some solution planes and part of the spectral element mesh used in the computations. The mesh extends 12.5 diameters upstream, 12.5 diameters above and below the cable, and 30 diameters downstream.

the normal component of the momentum equation. In the final stage, the viscous correction is computed and the updated velocity boundary conditions are applied:

$$\frac{\gamma_0 \boldsymbol{u}_m^{n+1} - \hat{\hat{\boldsymbol{u}}}_m}{\Delta t} = \frac{1}{Re} \left[\nabla_{xy}^2 - \beta^2 m^2\right] \boldsymbol{u}_m^{n+1}, \tag{2.18}$$

where γ_0 is the backwards differentiation coefficient in the stiffly stable scheme.

The modified flow equations (2.7) are solved using the Navier–Stokes code *Prism* developed by Henderson & Karniadakis (1995), which uses a mixed spectral element–Fourier discretization in the Eulerian reference frame. A similar code but without the transformation was used to investigate transition in the wake of the stationary cylinder by Karniadakis & Triantafyllou (1992). The discretization in the (x, y)-plane employs quadrilateral spectral elements, which are high-order finite elements with Legendre polynomials forming the expansion basis as tensor products in two dimensions. The mesh is shown in figure 4.

An important feature of the transformation is that it is divergence free, i.e. $\nabla \cdot \boldsymbol{\zeta} = 0$. This greatly reduces the number of extra terms generated by the transformation and

Case	N	NZ	$\bar{x}/d$	x'/d	y'/d	$\bar{C}_d$	C'_d	C_l	St
n7nz32	7	32	45.5364	0.0918	0.6683	2.00814	0.1586	0.3554	0.159
n9nz16	9	16	45.9742	0.1025	0.6792	2.02991	0.1682	0.3698	0.159
n9nz32	9	32	45.5213	0.0908	0.6677	2.00748	0.1588	0.3554	0.159
n9nz64	9	64	45.5213	0.0916	0.6677	2.00752	0.1586	0.3554	0.159
n11nz32	11	32	45.5218	0.0912	0.6677	2.00754	0.1588	0.3554	0.159

TABLE 1. Mesh resolution test: $L/d = 12.6$, $Re = 100$, $c = 2.1$, $\omega_n = 0.105$. Base case is n9nz32. N denotes spectral element polynomial order in the (x, y)-plane, and $NZ = 2M$ is the number of physical planes in the z-direction. Primes denote amplitudes and overbars denote time-averaged quantities. The number of spectral elements in the (x, y)-planes is 110.

makes the transformed equations look similar to the original equations, comparing the Navier–Stokes equations (2.1) to (2.7) and the continuity equation (2.2) to (2.8). The only additional work in solving for the flow is the computation of the acceleration terms $\boldsymbol{A}(\boldsymbol{u}, p, \boldsymbol{\zeta})$ which can be lumped with the nonlinear convective terms $(\boldsymbol{u} \cdot \nabla)\boldsymbol{u}$. The cable equations (2.15) are solved in Fourier space using the Newmark or average acceleration scheme, which is second-order accurate in time.

To verify the code and measure its accuracy we used two model problems, one to check temporal accuracy and stability, and the other to check spatial accuracy. Details of these validation tests are given in Newman (1996).

2.3. *Simulation parameters and parallel implementation*

The flow problem was computed using second-order-accurate time stepping and a quadrilateral spectral element–Fourier expansion in the (x, y)- and z-directions, respectively. Our study focuses on laminar ($Re = 100$) and transitional ($Re = 200$) wakes. We consider several periodic domain lengths (L/d) and initial conditions. In general, the cable is free to move in the streamwise and crossflow directions; however we sometimes constrain the cable to only allow motion in the crossflow direction. For all the cable simulations we ignored structural damping ($b = 0$).

Resolution tests were performed to check grid independence by varying the resolution both in the (x, y)-plane and the z-direction. Table 1 summarizes the results at $Re = 100$. We verify that our results are resolution independent at this Reynolds number. Similarly, selective tests at $Re = 200$ (reported also by Evangelinos & Karniadakis 1996) have verified the accuracy of the results presented here. However, the values of the measurements listed in the table may somewhat be affected by the blockage due to the relatively small size of the computational domain. This effect was found previously in simulations reported in Karniadakis & Triantafyllou (1992). Simulations in significantly larger domains would require excessive computational resources and produce little qualitative difference to the results.

The parallel implementation and benchmark results of the spectral element–Fourier code is described in Crawford *et al.* (1996). Because the linear contributions in the Navier–Stokes equations are decoupled in Fourier space, we assign each group of Fourier modes to a separate processor. The coupling, which comes from the advection and interaction terms, requires a global transpose of the data and multiple one-dimensional FFTs. Benchmarking of the parallel code *Prism* on a variety of computer platforms has shown that the IBM-SP2 is currently the most efficient and scalable computer for our code. The majority of our simulations were performed on our 24-node IBM-SP2 at the Center for Fluid Mechanics at Brown University and the IBM-SP2 at the Cornell Theory Center. Earlier simulations were performed

on the Intel-Paragons at the San Diego Supercomputing Center and at the Caltech Concurrent Supercomputing Facility. Typical simulations were run on 32 to 64 processors and took 1.5 s per time step on the IBM-SP2, and 6 s per time step on the Intel-Paragon. A non-dimensional time step of $U\Delta t/d = 0.002$ was used for most of the simulations, and integration times ranged from $Ut/d = 100$–1000 (i.e. 50 000–500 000 time steps).

3. Nonlinear flow-induced vibration response

To obtain a significant flow-induced vibration response we need to tune the natural frequency of one of the cable vibration modes to the frequency of vortex shedding. We use the fixed-cylinder shedding frequency to estimate this. For the Reynolds numbers in this study ($Re \leqslant 200$) the flow past a fixed-cylinder is two-dimensional (see Karniadakis & Triantafyllou 1992 and Barkley & Henderson 1996) and therefore this shedding frequency is easily measured from two-dimensional simulations.

In a forced linear spring–mass–damper system, the mass oscillates at the forcing frequency and the maximum response amplitude occurs when the forcing frequency is equal to the damped natural frequency. Flow-induced vibrations of a flexibly mounted cylinder are however highly nonlinear due to the fact that the cylinder motion affects the frequency and amplitude of the forcing, which in turn affects the cylinder motion. To quantify this effect we simulated the two-dimensional flow over an elastically mounted cylinder at $Re = 100$. At $Re = 100$, the Strouhal number of the fixed cylinder is $St = 0.167$, in agreement with the experimental results of Hammache & Gharib (1991). The cylinder has mass m, and is elastically mounted using a spring with stiffness k. The natural frequency $\omega_n = (k/m)^{1/2}$ is varied above and below the fixed-cylinder shedding frequency ω_0. The cylinder's response frequency, response amplitude, and forces on the cylinder are shown in figures 5(a), 5(b) and 5(c) respectively. All quantities are plotted against the ratio of the natural frequency to the fixed-cylinder shedding frequency ω_n/ω_0; here $\omega_0 = 2\pi f_0 = 1.05$. The lock-in regime is easily identified by the region of figure 5(a) where the response frequency depends linearly on the natural frequency. Outside this region, the cylinder vibration frequency tends towards the stationary cylinder shedding frequency, ω_0. Figure 5(b) shows that the maximum crossflow vibration amplitude is approximately $\eta/d \approx 0.6$, which occurs at $\omega_n/\omega_0 = 1.33$, i.e. 33% above the stationary-cylinder shedding frequency. The maximum streamwise amplitude is $\zeta/d \approx 0.05$ and occurs at about the same frequency. Figure 5(c) shows that the largest mean drag coefficient is $C_d = 2.3$, 60% larger than the stationary-cylinder mean drag coefficient of $C_d = 1.4$. The largest lift coefficient is $C_l' = 1.8$ and occurs at a slightly higher natural frequency of $\omega_n/\omega_0 = 1.5$. At that natural frequency the lift forces have a comparable magnitude to the drag forces.

Let us choose three of the flow-induced vibration cases to examine their wake structures. We select three natural frequencies where we observe a significant cylinder crossflow amplitude response; otherwise we would just see a wake very similar to the stationary cylinder-wake. The three cases chosen are spread across the natural frequency range: $\omega_n/\omega_0 = 0.75$, 1.0 and 1.33. In these three cases, the crossflow amplitude responses were $\eta/d = 0.2$, 0.5 and 0.6 respectively. Figure 6 shows instantaneous vorticity contours for these three natural frequencies. A reasonably regular wake is observed in all three cases and the increasing frequency of vortex shedding with increasing ω_n is obvious.

One of the most prominent differences in these three wakes is seen in the streamwise

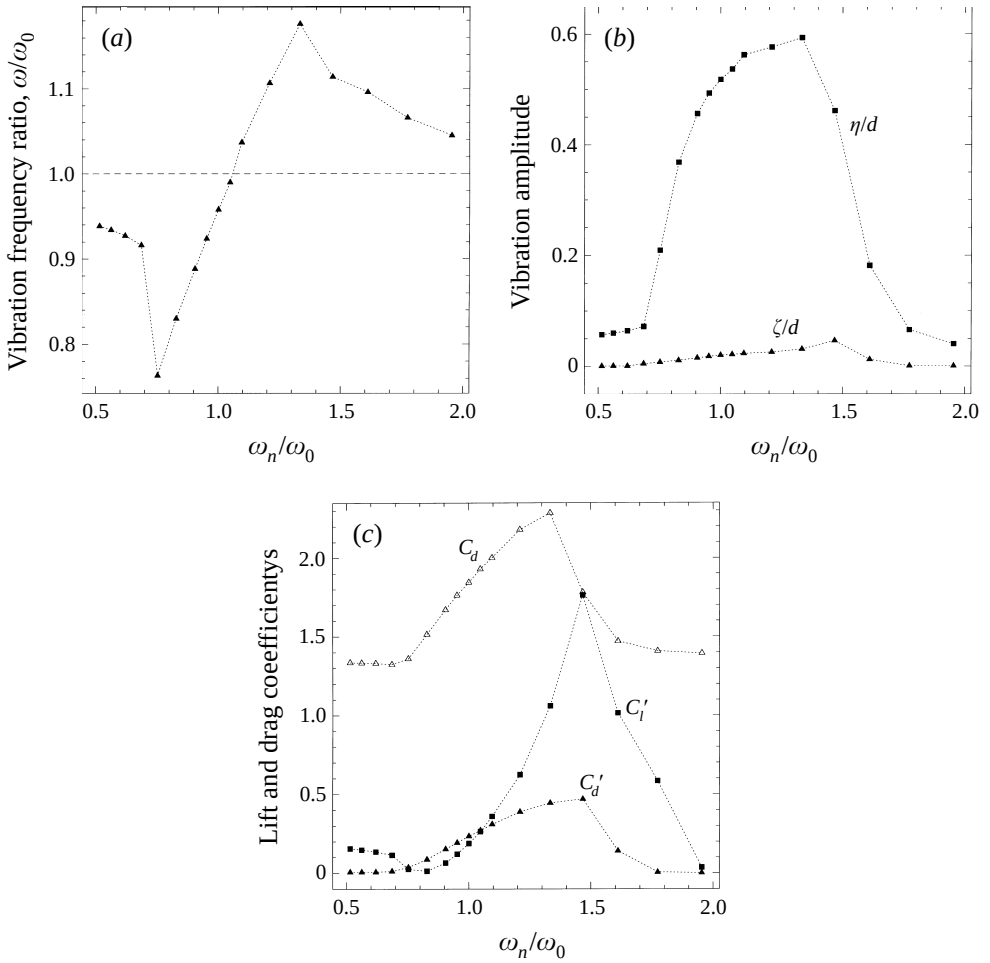

FIGURE 5. (*a*) Cylinder flow-induced vibration frequency, (*b*) cylinder flow-induced vibration amplitude (η/d: crossflow amplitude; ζ/d: streamwise amplitude), and (*c*) cylinder lift and drag coefficients (time-averaged and fluctuations), versus natural frequency normalized with fixed cylinder shedding frequency. Two-dimensional simulation at $Re = 100$.

and lateral spacing of the vortices. At $\omega_n/\omega_0 = 0.75$, these spacings are approximately $(7.25d, 1.6d)$, at $\omega_n/\omega_0 = 1.0$ the spacings are $(4.9d, 1.9d)$, and at $\omega_n/\omega_0 = 1.33$ the spacings are $(3.6d, 2.4d)$. In the last case, the aspect ratio of the lateral to streamwise vortex spacing ($2.4/3.6 = 0.67$) is much larger than the von Kármán limit for linear stability of an inviscid array of point vortices (approximately 0.28) or finite vortices (Saffman & Schatzman 1982 reports approximately 0.4). Therefore the primary vortex street is not stable, and this is evident in the last plot of figure 6, which shows the initial stage of this breakdown though the computational domain is not long enough to completely capture this process. A similar result has been observed by Brown, Karniadakis & Young (1993) in simulations with a backward-facing D-shaped cylinder when the vortex spacing aspect ratio exceeds 0.6. Also Ongoren & Rockwell (1988) have investigated in detail the large-scale structures downstream in a similar range of excitation frequencies for an oscillating circular cylinder and other cylinders of various cross-sections.

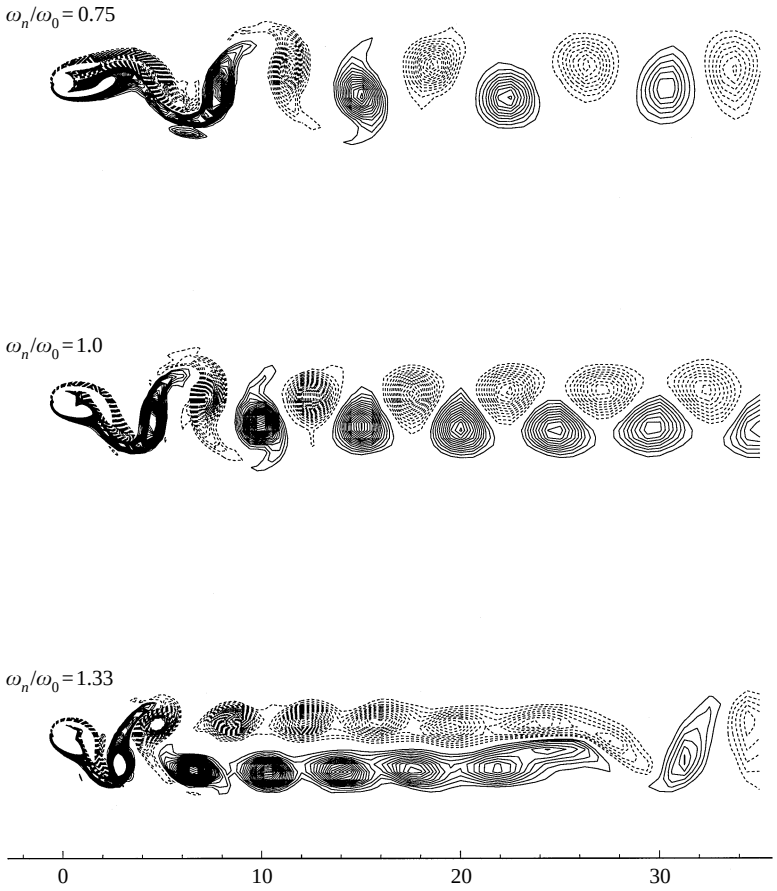

FIGURE 6. Flow-induced vibration simulations at $Re = 100$: instantaneous vorticity contours for natural frequency ratios $\omega_n/\omega_0 = 0.75, 1.0$ and 1.33.

4. Standing and travelling wave responses

The simplest periodic solutions to the vibrating string equation are standing waves and travelling waves. Both a standing wave response, $y(z,t) = A\cos(\omega t)\cos(2\pi z/L)$, and a travelling wave response, $y(z,t) = A\cos(\omega t \pm 2\pi z/L)$, satisfy the vibrating string equation, $y_{tt} = c^2 y_{zz}$, when $\omega = 2\pi c/L$, where c is the phase speed. In practice, both responses are observed in vibrating cables. Using data from field experiments, Vandiver (1991) has developed a simple criterion based on the product of the mode number and the modal damping ratio to determine which response will prevail.

In the simulations we can specify the initial conditions for the cable to be either a standing wave or travelling wave by specifying the cable's initial amplitude and velocity. Assuming that the forcing due to vortex shedding is at a frequency ω, for synchronization the appropriate cable tension is computed using $c = \omega L/(2\pi)$ where $c = (T/\rho)^{1/2}$. We choose ω to be the shedding frequency of a corresponding two-dimensional flow past a stationary cylinder at the same Reynolds number (i.e. $\omega = \omega_0$). We first discuss the $Re = 100$ results where the flow is laminar and three-dimensional.

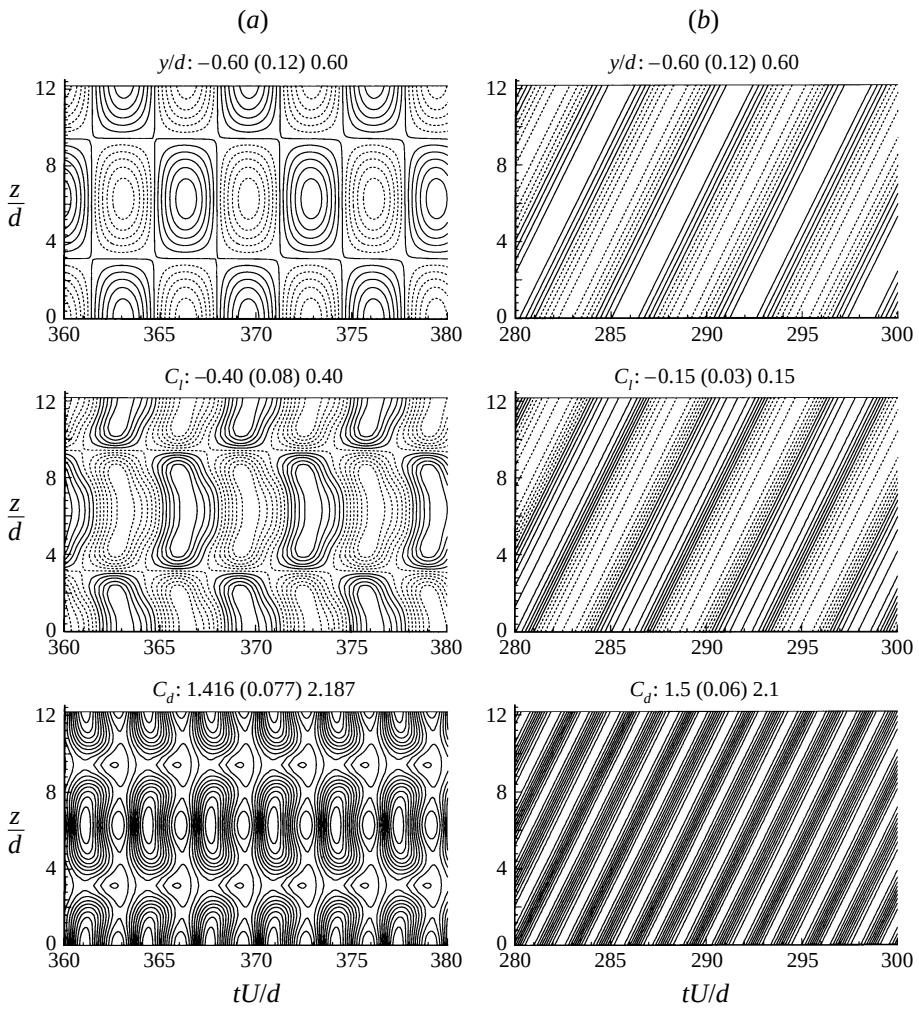

FIGURE 7. Cable crossflow displacement (y/d), lift coefficient (C_l) and drag coefficient (C_d) versus non-dimensional time and spanwise distance along cable for standing wave (*a*) and travelling wave (*b*) flow-induced vibration response, $L/d = 12.6$, $Re = 100$. Solid lines represent positive values, dashed lines represent negative values.

4.1. *Constrained cable*

Our first flow-induced cable vibration simulations consider the $Re = 100$ flow-induced vibration response to an initial standing wave and initial travelling wave of wavelengths $L/d = 6.3, 12.6, 18.8, 25.1$ at $Re = 100$. For these simulations, the cable is *constrained* to only allow motion in the crossflow direction. Not only is this the primary direction of cable vibration, but it is an easier case to initially consider because the unconstrained cable has a longer time transient for the cable to settle down to a mean downstream position. Each simulation started with a three-dimensional $Re = 100$ wake flow and the cable having the appropriate initial displacement and velocity for the standing wave or travelling wave. All of these simulations converge to a time-periodic cable response and flow field within about ten shedding periods.

We first study the response for the $L/d = 12.6$ wavelength vibration case. In figure 7, we plot crossflow cable displacement y/d, lift coefficient C_l, and drag

Case	y/d	C_l	$\bar{C}_d$	C'_d	St
Fixed	-	0.34	1.37	0.01	0.167
2-d Free	0.52	0.20	1.85	0.23	0.160
Standing	0.69	0.50	1.72	0.46	0.153
Travelling	0.50	0.16	1.78	0.28	0.161

TABLE 2. Results for two-dimensional and standing and travelling wave cases for cable maximum amplitude (y/d), maximum lift (C_l), mean and fluctuating drag coefficient ($\bar{C}_d, C'_d$), and vibration frequency. $L/d = 12.6$, $Re = 100$.

coefficient C_d, versus dimensionless time tU/d, and position along cable z/d. We define the force coefficients in the usual manner. For example, given a lift force F_l, we define the lift coefficient as $C_l = F_l/\frac{1}{2}\rho_f dLU^2$. Note that we use coordinate y to mean cable displacement η (and similarly for x and ζ). Figure 7 shows the plots for the $L/d = 12.6$ standing wave (a) and travelling wave (b) flow-induced vibration responses for approximately three shedding cycles. The initially specified standing wave case converges to a state where the cable motion is a sustained standing wave with crossflow amplitude $y/d = 0.69$ and frequency $f = 0.153$. This frequency is slightly lower than the shedding frequency for the fixed cylinder ($f_0 = 0.167$) in the two-dimensional simulations; this observation is consistent with the models described in Sarpkaya (1979). The lift coefficient shows a similar pattern to the cable motion, with the lift force being almost in phase with the cable motion. Note also that the lift force at the nodes of the standing wave is always zero due to the antisymmetry of wake structure, which induces a symmetric distribution of pressure and viscous stresses on the cable. The drag coefficient is periodic with twice the frequency of the lift coefficient, because the drag does not differentiate between shedding of opposite-sign vortices.

The corresponding travelling wave plots on figure 7(b) show that all three variables are moving with a constant wave speed (in the positive z-direction) equal to the phase speed $c = 2.1$. The crossflow displacement has an amplitude $y/d = 0.50$, which is significantly smaller than the amplitude observed in the standing wave case. The frequency of oscillation is $f = 0.161$, also different from the fixed cylinder and standing wave cases. More importantly, the magnitude of the lift coefficient in this travelling wave case is about one third of that measured in the standing wave case. The mean drag coefficients are approximately the same for the standing wave and travelling wave vibration cases. Again, the relative phases of the travelling wave cable motion and the forces are similar to those observed in the standing wave case, with the motion just slightly lagging the force.

These results are summarized in table 2, listing the two-dimensional cases and the $L/d = 12.6$ wavelength vibration cases. We see that the maximum values for the displacement, lift and drag coefficients are all observed for the standing wave case. Note that the results for the travelling wave are similar to those for the two-dimensional free cylinder case. The mean drag coefficients for the standing and travelling wave flow-induced vibration cases are $\bar{C}_d = 1.72$ and $\bar{C}_d = 1.78$ respectively, approximately 25% larger than the mean drag coefficient for the fixed cable ($\bar{C}_d = 1.37$).

A comparison of vibration amplitudes and forces as a function of vibration wavelength (L/d) for standing wave and travelling wave vibration is given in table 3 for four vibration wavelengths. We see that for both the standing wave and travelling

Case	L/d	y/d	C_l	$\bar{C}_d$	C'_d	St
Standing wave	6.3	0.65	0.73	1.60	0.30	0.147
	12.6	0.69	0.50	1.72	0.46	0.153
	18.8	0.68	0.47	1.73	0.51	0.156
	25.1	0.68	0.52	1.73	0.52	0.159
Travelling wave	6.3	0.30	0.38	1.55	0.20	0.154
	12.6	0.50	0.16	1.78	0.28	0.161
	18.8	0.50	0.16	1.83	0.33	0.161
	25.1	0.50	0.20	1.82	0.36	0.164

TABLE 3. Constrained standing and travelling wave amplitude, force coefficients and frequency results for $L/d = 6.3$, 12.6, 18.8 and 25.1, at $Re = 100$.

L/d	Angle (deg.)
6.3	42*
12.6	21
18.8	10
25.1	5

TABLE 4. Oblique vortex shedding angle versus cable wavelength for travelling wave responses. Constrained cable at $Re = 100$. Note: * denotes the case where travelling response wave broke down to a standing wave response.

wave flow-induced cable responses, the motion and forces are generally insensitive to spanwise cable vibration wavelengths L/d from 12.6 to 25.1. Slight exceptions to this insensitivity are larger lift coefficients and maximum drag coefficients for the longest wavelength. For both the standing wave and travelling wave, we see a significant difference for the shortest vibration wavelength of $L/d = 6.3$, probably due to the particularly large curvature in the cable for this relatively short vibration wavelength. In every case, except the $L/d = 6.3$ travelling wave, the resulting motion maintains its form, i.e. standing waves remain standing waves, and travelling waves remain travelling waves, and this motion remains periodic in time, over several shedding periods. The time-asymptotic response, however, may be different. In particular, in the $L/d = 6.3$ travelling wave case the cable response eventually changes to a standing wave cable response. This change in crossflow displacement response is shown in figure 8, and is due to the angle of oblique vortex shedding being too large. Table 4 lists the angle of oblique vortex shedding for the four vibration wavelengths. We see that the angle is inversely proportional to the wavelength. For L/d=6.3, the angle 42° is too large to be sustained, and the flow-induced travelling wave cable response breaks down to a standing wave cable response, as seen in figure 8.

At $Re = 100$, flow over a cylinder is two-dimensional, and we see parallel vortex shedding. If we take a slice of the flow field perpendicular to the cylinder, we see the well-known von Kármán vortex street pattern of staggered vortices with alternating signs. A top view of this wake, looking in the negative y-direction, shows parallel rolls of vorticity being shed from the cylinder and convecting downstream. Starting with the familiarity of the wake structure in this simple case, we now plot iso-contours of spanwise vorticity in the wakes of the flow-induced standing and travelling waves. Figures 9 and 10 show a top view and perspective view of equal and opposite levels of spanwise vorticity ($\omega_z = \pm 0.2$) for the standing and travelling wave cable wakes respectively for the $L/d = 12.6$ vibration case. The darker shade shows negative

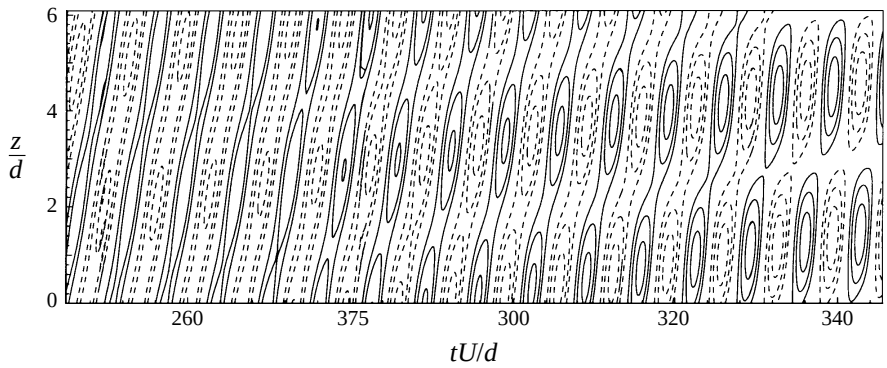

FIGURE 8. Contours of cable crossflow displacement showing the breakdown of a travelling wave response to a standing wave response for $L/d = 6.3$, $Re = 100$.

spanwise vorticity and the lighter shade shows positive spanwise vorticity. The flow is from left to right, and the cable is located at $x = 0$. We see a remarkably different structure of the wake flow depending on the cable response. The standing wave cable response produces an interwoven structure to the spanwise vorticity. In contrast, the travelling wave cable response produces oblique shedding of spanwise vorticity, i.e. much like the shedding in the fixed cylinder case, but at an angle to the spanwise direction. Oblique shedding has been observed in flows over fixed cylinders in many experimental studies (see for example, Hammache & Gharib 1991 and Eisenlohr & Eckelmann 1989). The standing wave plots show that the 'nodes' (location of zero cable displacement) of the cable are located at the two ends and middle of the cable in the figure ($z = 0$, 6.3 and 12.6, respectively). In the case of the travelling wave, the nodes move in the negative z-direction at the phase velocity c.

Further differences between the structure of the wakes behind travelling and standing wave vibrating cables are shown by looking at spanwise velocity. Figures 11(a) and 11(b) show contours of spanwise velocity in a slice through the flow field at downstream distance $x/d = 10$, for the standing wave and travelling wave, respectively. In the standing wave case we see that the spanwise velocity is zero at the anti-nodes of the cable. This means that no fluid crosses the (x, y)-planes through the anti-nodes. In contrast, for the travelling wave, we see that fluid is moving in both positive and negative spanwise directions, indicating a greater spanwise mixing of the fluid.

We can obtain further insight into the structure of the wake by looking at slices of the flow field perpendicular to the cable. For this purpose, we take slices at four spanwise positions: the cable maximum (anti-node), node, minimum (anti-node) and subsequent node. Figures 12 and 13 show spanwise vorticity at these slices for the $L/d = 12.6$ standing wave and travelling wave vibration cases, respectively. Dotted contour levels indicate negative values. This view highlights the difference in the wake structure between the standing and travelling wave wakes. In the standing wave case, we see a very different pattern of spanwise vorticity in the wake behind the nodes compared to the wake behind the anti-nodes. It appears that vortices are shed simultaneously at this location, similar to what is sometimes observed in experiments with in-line oscillations, as reported by Sarpkaya (1979). Behind the anti-nodes we see a relative large lateral spacing of vortices. The shedding patterns between successive anti-nodes are antisymmetric with respect to one another, consistent with

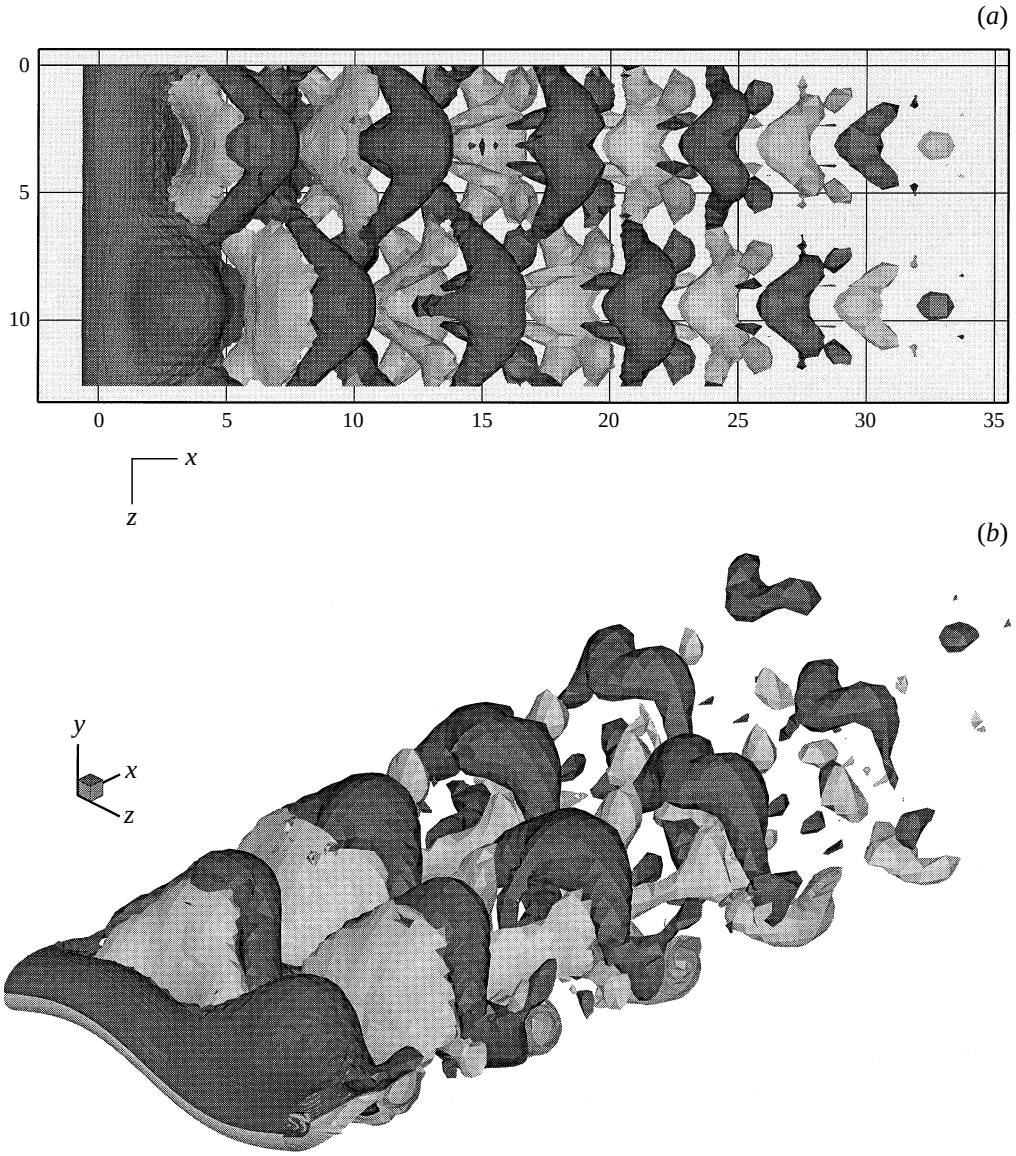

FIGURE 9. Top and perspective views of spanwise vorticity for the standing wave cable response. The two shades denote equal and opposite magnitude of spanwise velocity, contour levels $\omega_z = \pm 0.2$, $Re = 100$.

the interwoven picture of the perspective view; in contrast, the patterns behind the two nodes are identical.

In the travelling wave case (figure 13), the plots at the four spanwise positions look more similar to one another. Each wake pattern looks relatively similar to the two-dimensional fixed cylinder. These four plots show phases at 1/4 cycle intervals. Consequently, plots (*a*) and (*c*) are antisymmetric, and plots (*b*) and (*d*) are antisymmetric with respect to one another. Phases in time are indistinguishable from phases in space (i.e. position along the cable), because we have a travelling wave solution of $\phi(z + ct) = \text{const}$. Also, the magnitude of streamwise vorticity is higher

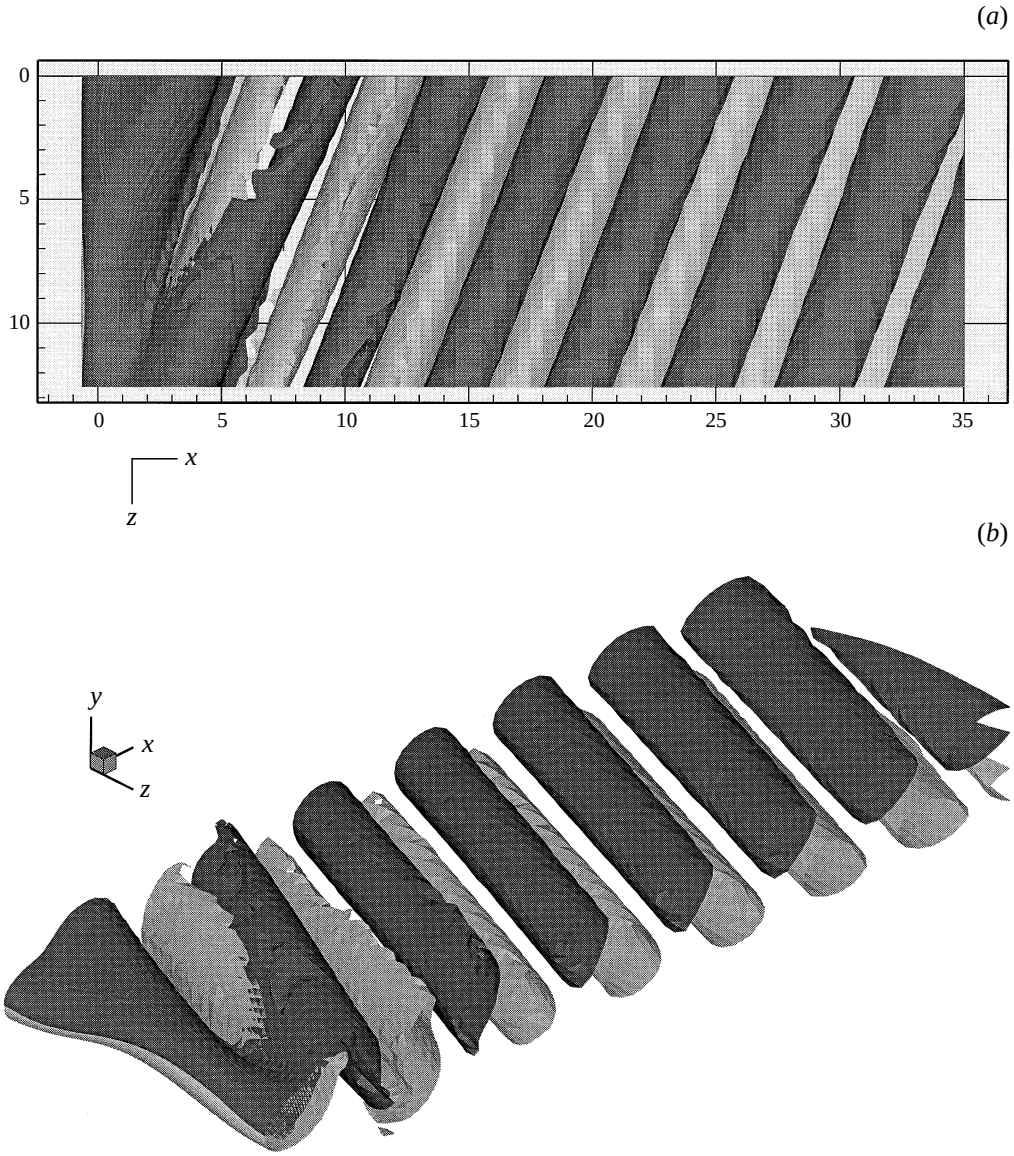

FIGURE 10. Top and perspective views of spanwise vorticity for the travelling wave cable response. The two shades denote equal and opposite magnitude of spanwise velocity, contour levels $\omega_z = \pm 0.2$, $Re = 100$.

as a function of downstream distance, than that in the standing wave wake. This is partly due to the greater coherence of the structure of vorticity in oblique shedding. The streamwise spacing of vortices is approximately 6 diameters in the standing wave case, and approximately 5 diameters in the travelling wave case.

An obvious difference between the wake in both the standing and travelling wave flow-induced vibration cases with the wake behind a fixed cylinder (all at $Re = 100$) is that the former wakes are intrinsically three-dimensional, while the wake behind the fixed cylinder is two-dimensional. Consequently, the streamwise and normal vorticities (ω_x and ω_y) will be non-zero in the three-dimensional case. Figure 14 shows a top view

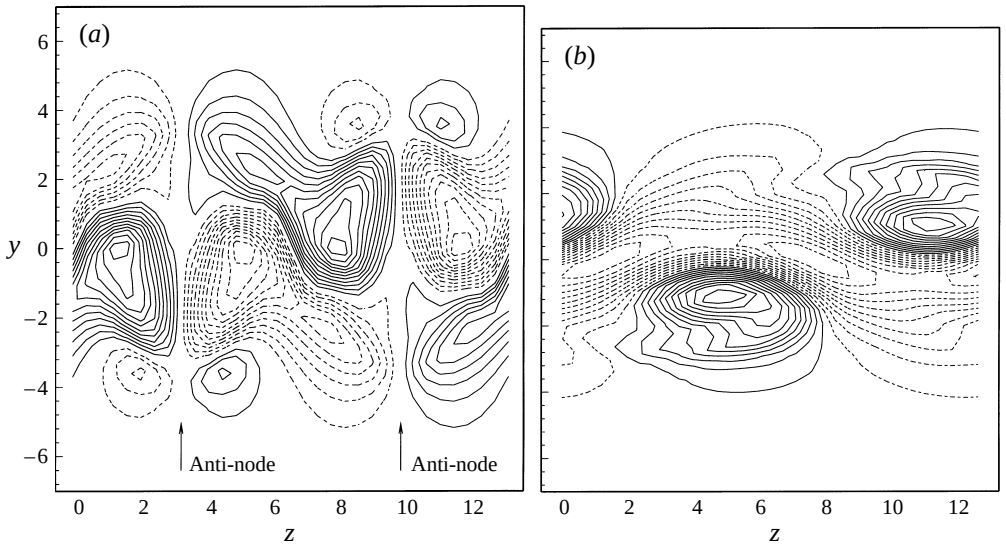

FIGURE 11. Spanwise velocity in the (y, z)-plane behind (*a*) a standing wave and (*b*) a travelling wave, at $x/d = 10$, $Re = 100$.

of the three vorticity components for the standing wave (*a*) and travelling wave (*b*) wakes. The two shades denote equal and opposite levels of the vorticity, and the same contour levels ($\omega = \pm 0.2$) are used in all the plots to allow easy comparison. Looking first at the standing wave wake, we see that the cable vibration introduces significant streamwise vorticity; in fact further downstream, the streamwise vorticity is the largest of the three vorticity components. The magnitude of this streamwise vorticity should be related to the ratio of the cable vibration amplitude to the wavelength since this is a direct means of introducing streamwise rotation into the flow. The streamwise and normal vorticities are zero in the planes of the anti-nodes. Again, we see the staggered pattern of spanwise vorticity shown previously in figure 9. Now looking at the top view of the three vorticity components of the travelling wave wake (figure 14*b*), we see a similar picture for the three components. Note in this travelling wave case that further downstream, the largest vorticity component is spanwise vorticity. Given a vorticity magnitude of ω, the streamwise and spanwise vorticity components approximately will be $\omega_x = \omega \sin\theta$ and $\omega_z = \omega \cos\theta$ respectively, where θ is the shedding angle. The normal vorticity ω_y in this case decreases rapidly with downstream distance.

We make one final observation before moving onto the unconstrained cable flow-induced vibration simulations. Although the standing wave cable response is sustained for several shedding periods, we observe that eventually (after more than 20 shedding periods) this standing wave response gradually becomes a travelling wave response, for the $L/d = 12.6$ vibration wavelength case. This change in response is shown in figure 15, where we see primarily a standing wave response at $tU/d = 500$, and primarily a travelling wave response at $tU/d = 570$ (over an interval of approximately 11 shedding cycles). This is consistent with observations in field experiments with very long cables by Vandiver (1991), and Alexander (1981) where no reflections are possible from the cable's ends due to amplitude attenuation along the cable. Therefore, the infinite-cable behaviour prevails in this case, as it does in our simulations.

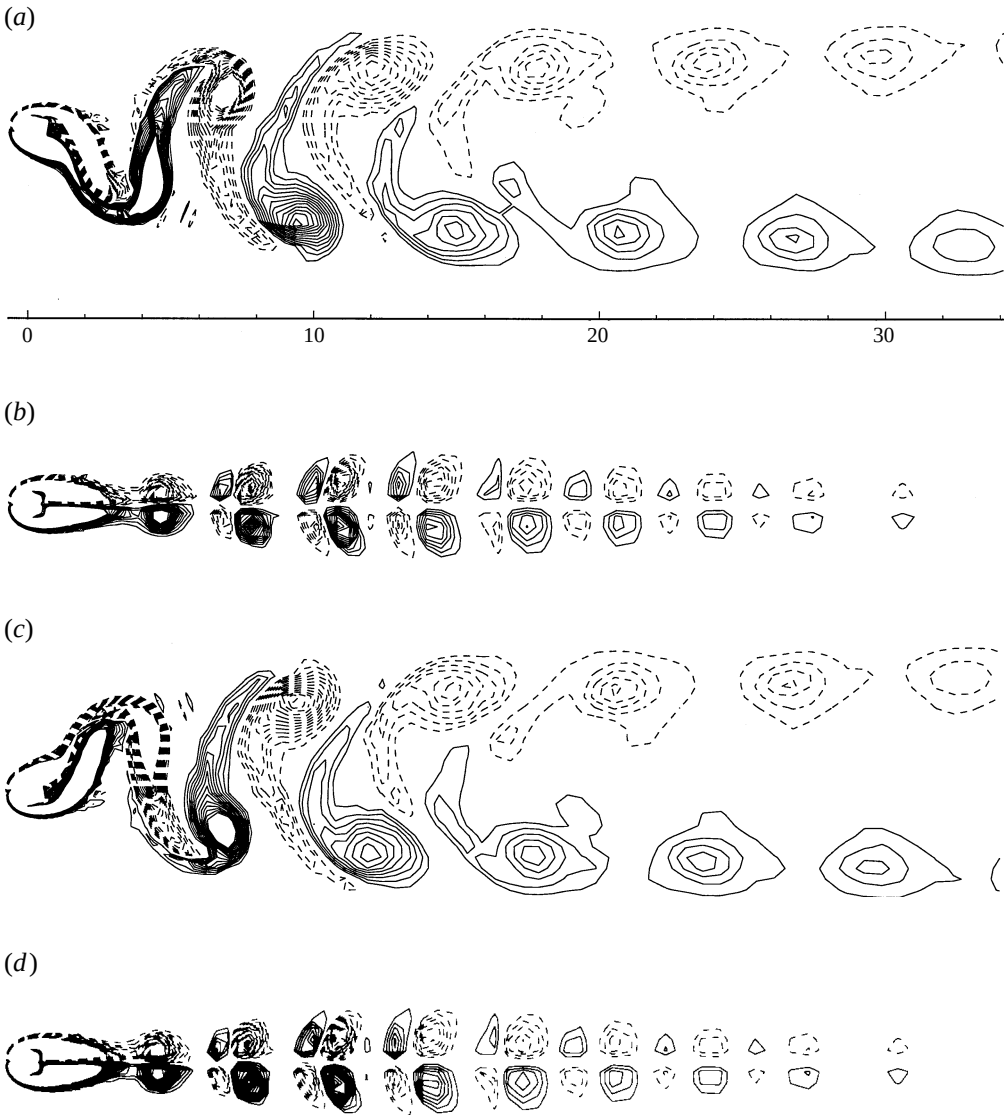

FIGURE 12. Slices in the (x, y)-plane showing spanwise vorticity for the standing wave case: at (a) the cable anti-node (max), (b) node, (c) anti-node (min) and (d) node. $Re = 100$.

4.2. *Unconstrained cable*

In all the flow-induced vibration simulations in the previous section, the cable was constrained to only allow motion in the crossflow direction. This constrained case was simpler and it involved a shorter transient for the cable and flow response to reach a time periodic state. In this section, we consider the flow-induced vibration of a completely free cable, allowing motion in both the streamwise and crossflow directions. We concentrate on the vibration wavelength $L/d = 12.6$, but also consider longer wavelengths up to $L/d = 201.1$. The assumption of an infinitely long spanwise-periodic cable introduces a small computational problem. Because the cable has no end conditions (e.g. pinned ends) there is no means of maintaining a mean streamwise cable position to balance the mean drag force. A convenient solution is to introduce

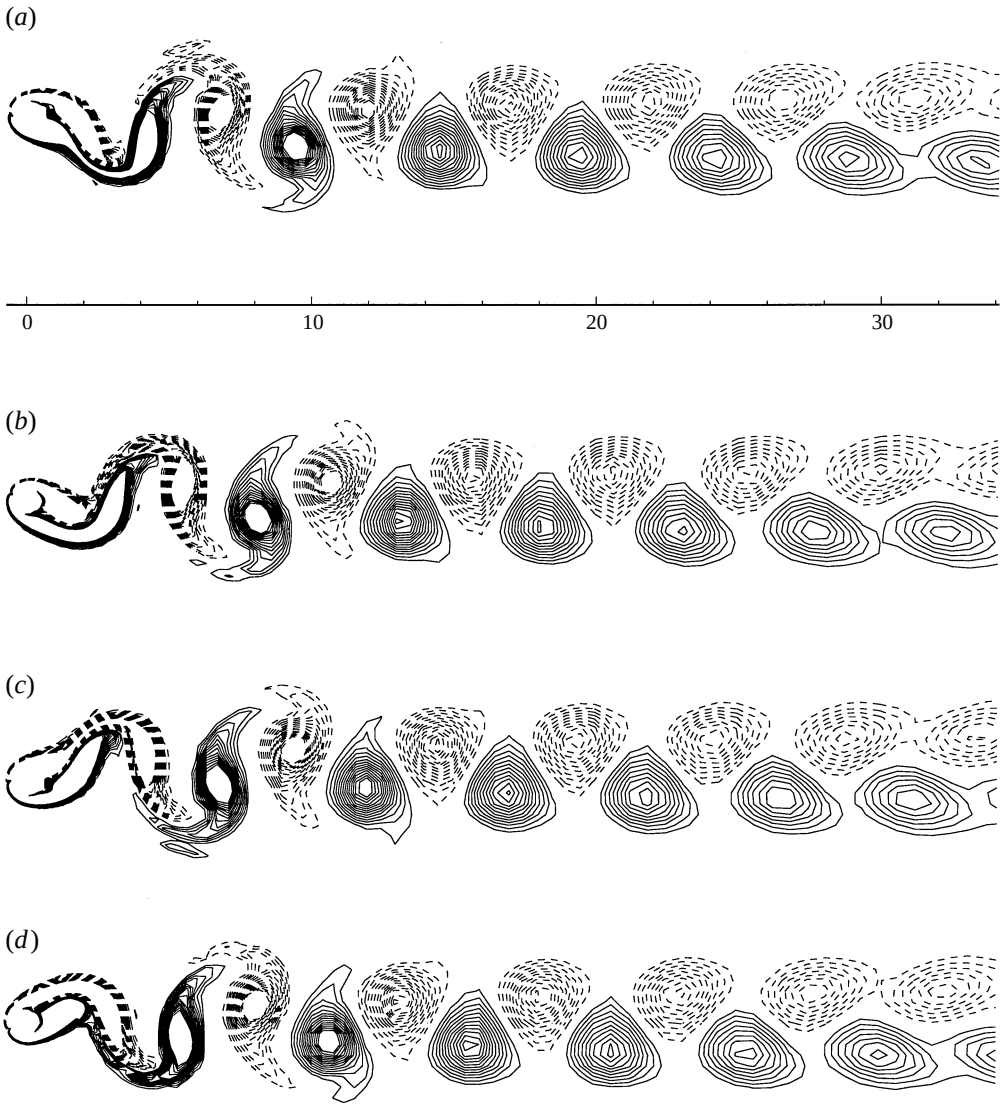

FIGURE 13. Slices in the (x, y)-plane showing spanwise vorticity for the travelling wave case: at (*a*) the cable anti-node (max), (*b*) node, (*c*) anti-node (min) and (*d*) node. $Re = 100$.

a ficticious light elastic support that runs the length of the cable. Using a spring with stiffness per unit length k, and given the cable mass per unit length ρ, we get a mode-zero natural frequency $\omega_n = (k/\rho)^{1/2}$. So in each direction of motion, we model the cable equation with

$$\zeta_{tt} + \omega_n^2 \zeta = c^2 \zeta_{zz} + (1/\rho) F_d(z, t). \tag{4.1}$$

We choose a spring constant k, such that the natural frequency of the first mode of vibration increases by no more than 0.5%. If we assume a homogeneous solution $\zeta = \mathrm{e}^{\mathrm{i}(\omega_m t + 2\pi m z/L)}$, by substituting this into the unforced version of (4.1), for mode $m = 1$ we get, $-\omega_1^2 + \omega_n^2 = -c^2(2\pi/L)^2$, i.e. choose $\omega_n \approx 0.1 \times 2\pi c/L$ to limit the increase in ω_1 to less than 0.5%. The effect of the elastic support is less with higher

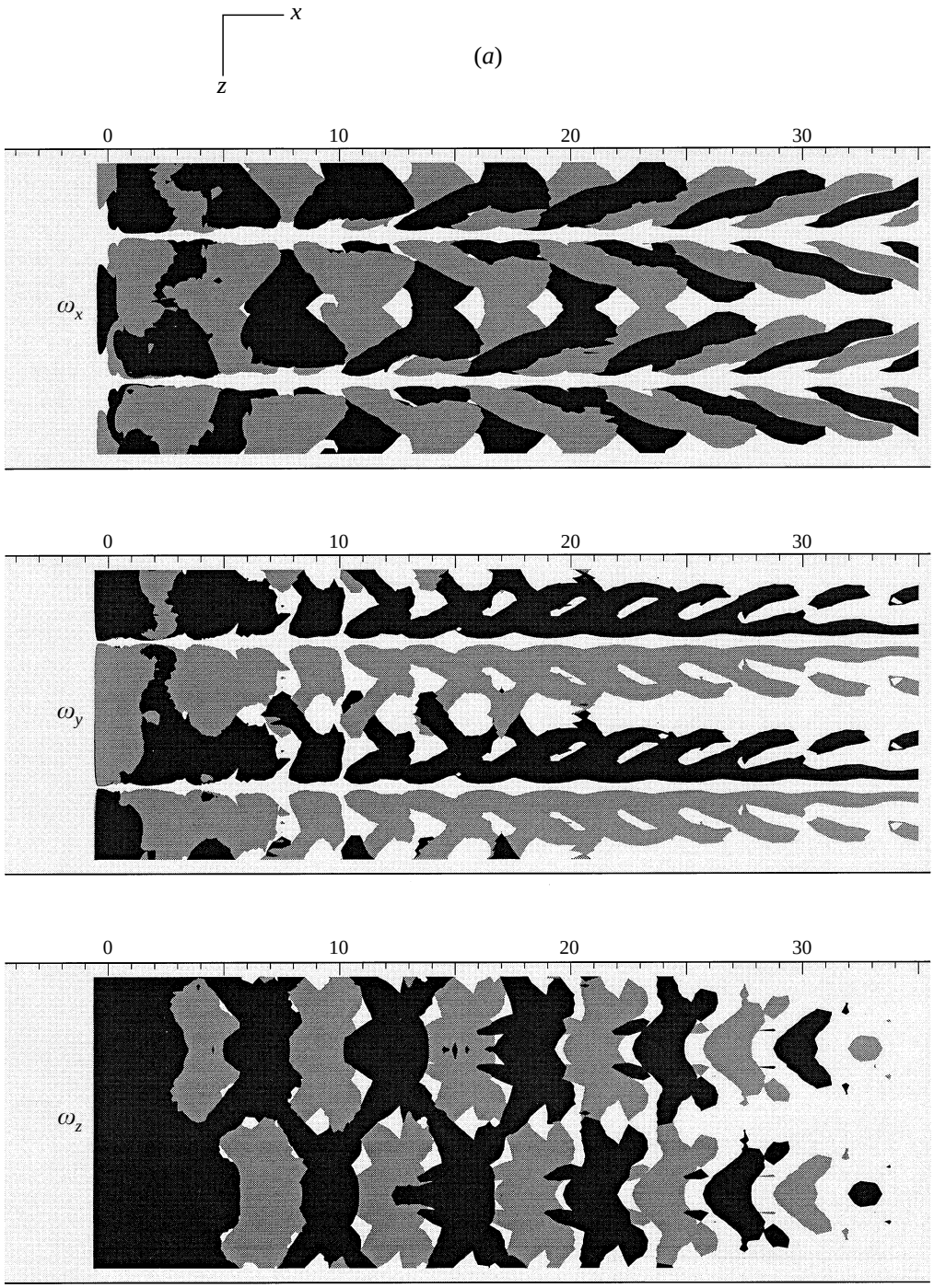

FIGURE 14(*a*). For caption see facing page.

(*b*)

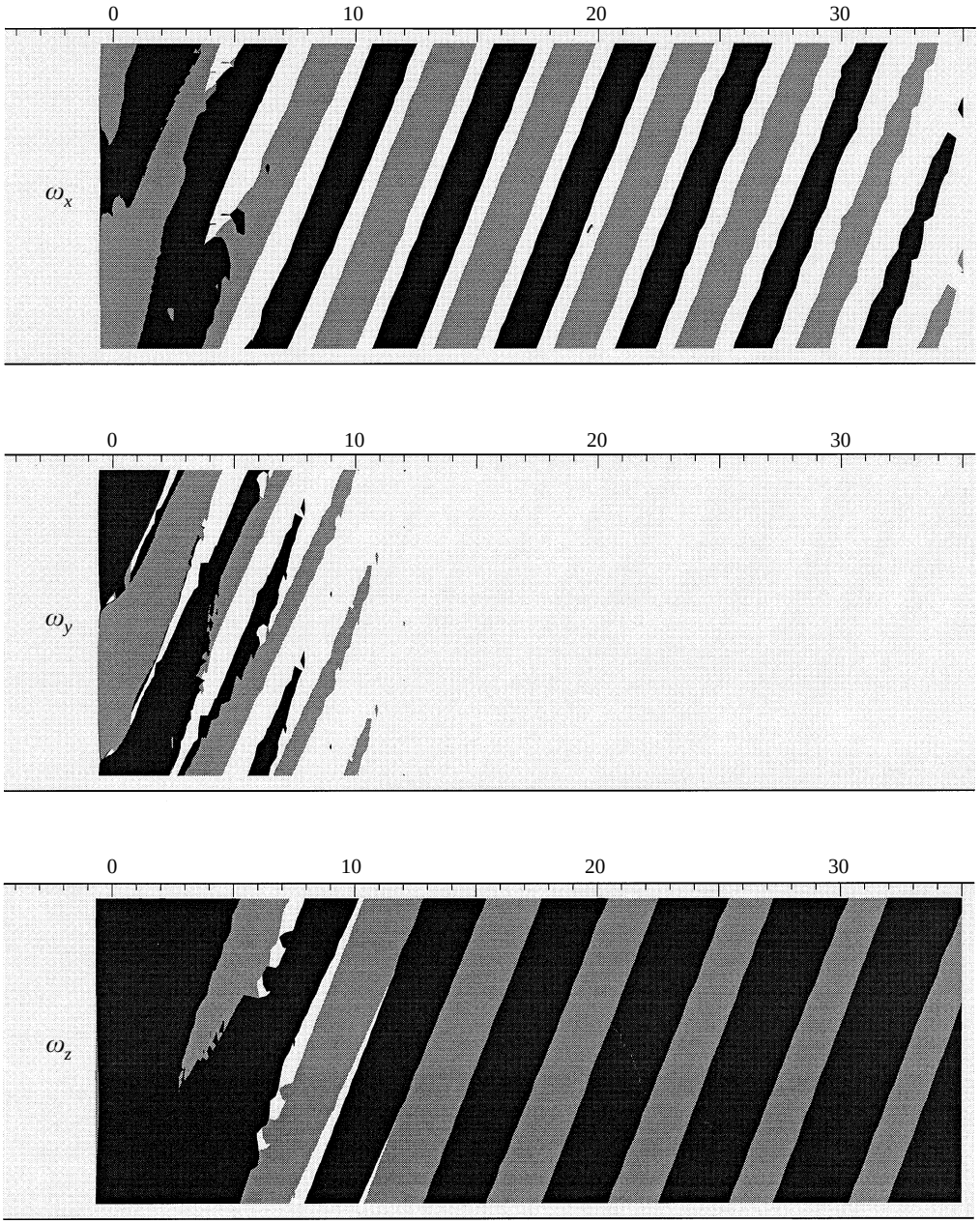

FIGURE 14. Top view of three vorticity components for wake behind a constrained standing wave (*a*) and travelling wave (*b*), $Re = 100$. Contour levels $\omega = \pm 0.2$.

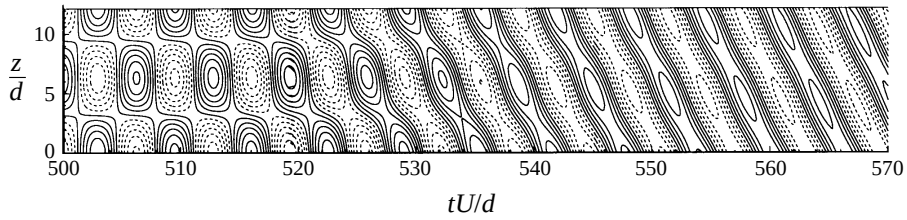

FIGURE 15. Contours of cable crossflow displacement showing the constrained standing wave cable response eventually becoming a travelling wave response after many shedding periods, $Re = 100$.

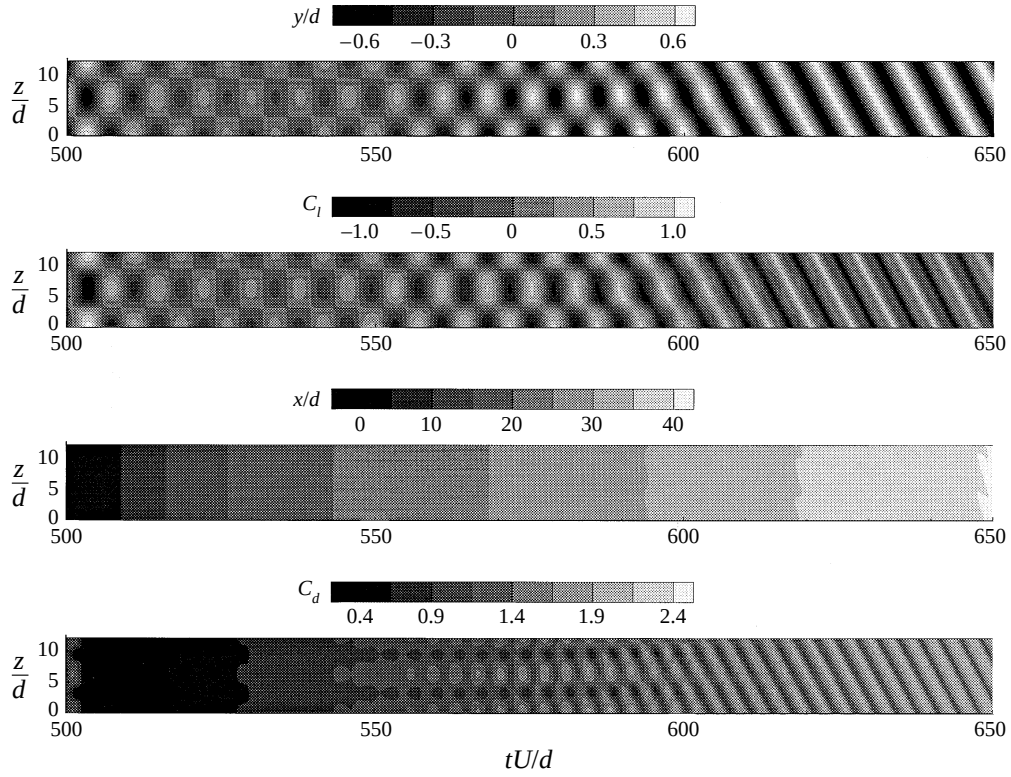

FIGURE 16. Contour plots of cable crossflow displacement, lift coefficient, streamwise displacement and drag coefficient, showing the immediate breakdown of a standing wave response to a travelling wave response when the streamwise motion constraint is removed, $Re = 100$, $L/d = 12.6$.

modes – for example the frequency of mode $m = 2$ is increased by only 0.1%. The spring constant is given by $(k/\rho)^{1/2} = 0.1 \times 2\pi c/L = 0.105$, so $k = 0.02$. Therefore, the mean streamwise position of the cable is approximately $\bar{x} = \bar{F}_d/k = 0.9/0.02 = 45$ diameters downstream.

Two $L/d = 12.6$ unconstrained cable simulations are run, starting with the standing wave and travelling wave fields obtained in the previous section. The simulations are run until a time-periodic state is reached. We observe that the standing wave cable response quickly becomes a travelling wave cable response, as is seen in figure 16. The streamwise motion constraint is removed at $tU/d = 500$. At $tU/d = 650$, the position

L/d	y/d	C_l	$\bar{C}_d$	C'_d	St
12.6	0.668	0.355	2.008	0.159	0.159
25.1	0.733	0.599	2.039	0.303	0.156
50.3	0.794	0.938	2.230	0.572	0.152
100.5	0.793	0.968	2.238	0.598	0.150
201.1	0.793	0.957	2.245	0.591	0.151

TABLE 5. Longer-wavelength unconstrained flow-induced vibration case results, $Re = 100$.

of the cable is approximately 40 diameters downstream from where it started (third plot). At this time the travelling wave cable response is clearly seen. The direction of motion of this travelling wave (whether $+z$ or $-z$) is arbitrary; in this case we see a travelling wave in the $-z$-direction. Since the responses of the cable with both the standing wave and travelling wave initial conditions become the same, we only need to report on one, which we refer to as the unconstrained travelling wave response, or just the flow-induced vibration response.

Figure 17(*a*) shows the cable's crossflow displacement y/d, lift coefficient C_l, streamwise displacement x/d, and drag coefficient C_d, versus time tU/d, and position along cable z/d, for this unconstrained travelling wave. Comparing these results with the constrained travelling wave plots in figure 7, we see that the cable's streamwise motion x/d oscillates with twice the frequency and half the spanwise wavelength of the crossflow motion y/d. Furthermore, the amplitude of the cable vibration in the streamwise direction is approximately $x/d = 0.09$, less than 15% of the crossflow vibration amplitude of $y/d = 0.67$. To check for any differences in flow structure with the constrained case, we also plot slices of spanwise vorticity. Figure 17(*b*) shows the slices at four equispaced positions along the cable. The pattern of spanwise vorticity is almost the same as in figure 13, except for a slight difference in the coalescence of same-sign spanwise vorticity at approximately 20 diameters downstream.

Finally, we study how the unconstrained cable vibration response varies with increasing vibration wavelengths from $L/d = 12.6$ to 201.1. Table 5 summarizes the cable crossflow amplitude and force results. The amplitude of cable vibration increases almost 20% from $y/d = 0.668$ to $y/d = 0.794$ as the vibration wavelength increases. Along with this we see a more than a twofold increase in the amplitude of the lift coefficient, but only a 10% increase in the mean drag coefficient. The vibration frequency drops by approximately 5% in the longer-wavelength cases.

4.3. *Sensitivity to cable tension*

In all the simulations presented, the tension of the cable (i.e. phase speed) was chosen so that the natural frequency of the cable vibration matched the corresponding shedding frequency of flow past a stationary cylinder at $Re = 100$. To investigate the sensitivity of cable motion and forces to cable tension, additional simulations were run for the unconstrained travelling wave at 10% lower phase speed (20% lower cable tension), and 10% higher phase speed (20% higher cable tension). As a base case we considered the simulation at $Re = 100$, $L/d = 12.6$, and $c = 2.1$. The results are listed in table 6. The higher phase speed produces larger vibration amplitude, lift coefficient and mean and fluctuating drag coefficient. A similar result was also observed in our two-dimensional simulations.

(*a*)

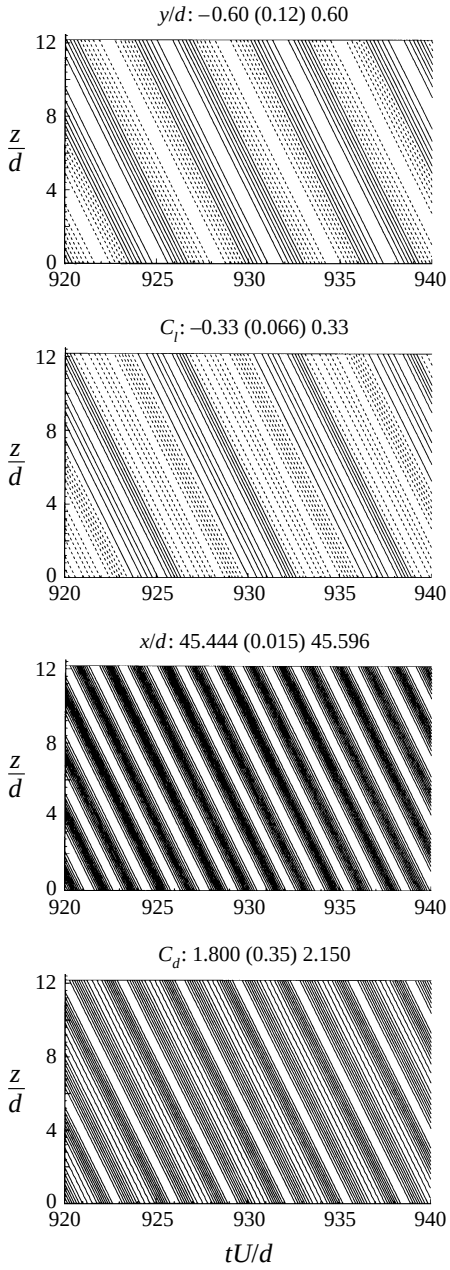

FIGURE 17(*a*). For caption see facing page.

4.4. *Response to random initial conditions*

We are interested in further investigating the preferred time-asymptotic vibration response of a cable undergoing flow-induced vibration. In the previous section, we found that for a constrained cable, both standing wave and travelling wave vibration modes are relatively stable over several shedding periods. In those cases, the initial

(*b*)

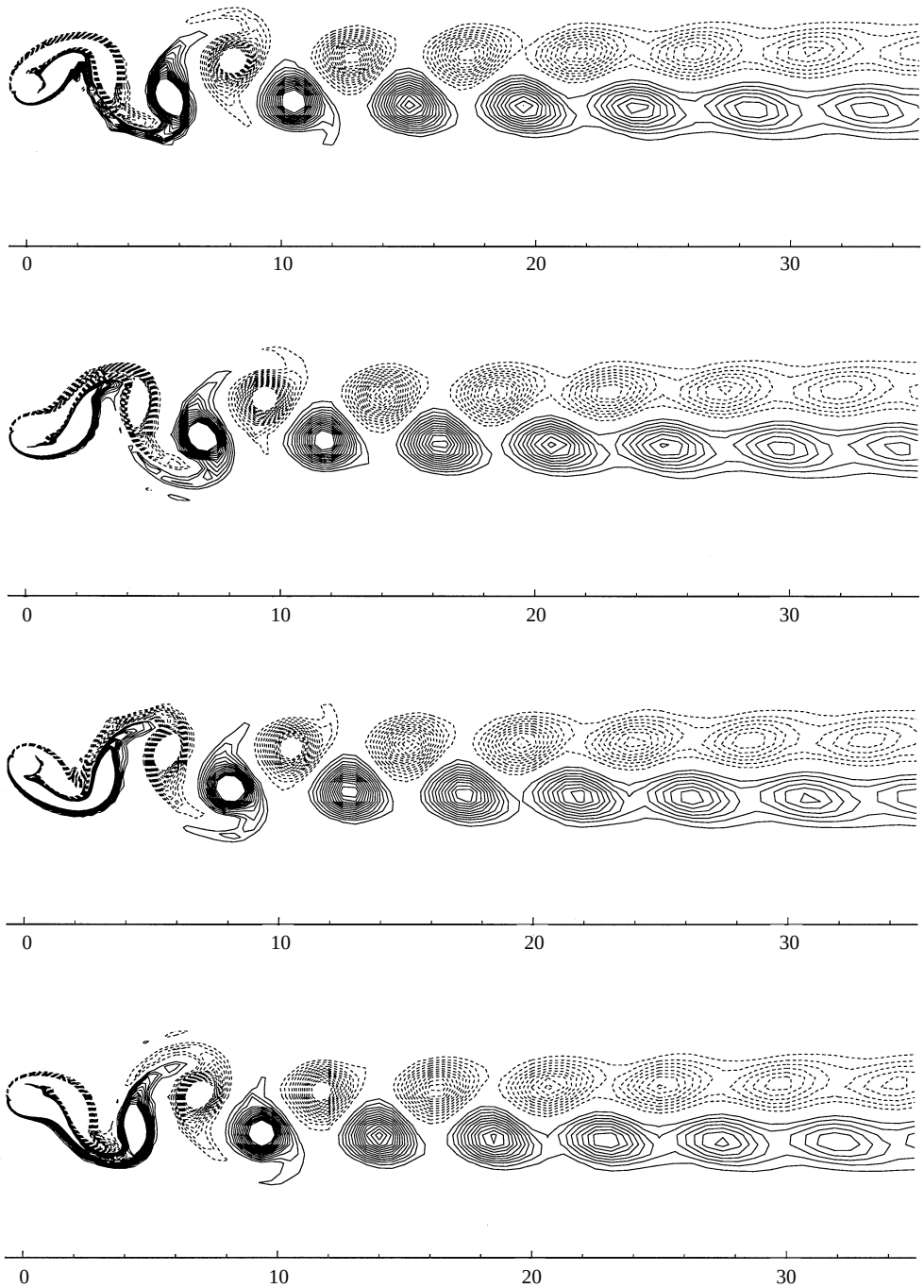

FIGURE 17. (*a*) Cable crossflow displacement (y/d), lift coefficient (C_l) and drag coefficient (C_d) versus non-dimensional time and spanwise distance (z/d) along the cable for unconstrained travelling wave response $L/d = 12.6$. (*b*): Slices in the (x, y)-plane showing spanwise vorticity for the unconstrained travelling wave case. From top to bottom the plots show the slices at the cable anti-node (max), node, anti-node (min) and node, respectively. $Re = 100$.

c	y/d	C_l	$\bar{C}_d$	C'_d	St
1.9	0.567	0.158	1.745	0.051	0.144
2.1	0.668	0.355	2.007	0.159	0.159
2.3	0.737	0.750	2.257	0.419	0.174

TABLE 6. Sensitivity of cable motion and forces on cable tension, $L/d = 12.6$, $Re = 100$. Base case is unconstrained travelling wave, $c = 2.1$.

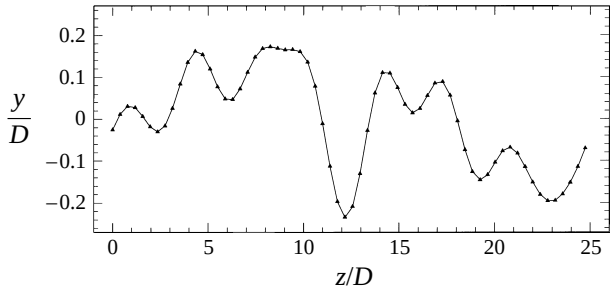

FIGURE 18. Quasi-random initial cable displacement; initial cable velocity is zero.

cable position and velocity were prescribed as a standing wave and travelling wave. The resulting cable motion for these two cases was primarily single-moded responses of a standing wave and travelling wave respectively (although, recall, that after a very long time the standing wave response changed to a travelling wave response). Now we raise the question: Is a multi-moded vibration response possible, and under what conditions do we get such a response? To try to answer this question, we performed simulations with the cable having a quasi-random initial position and zero initial velocity. In this way, we let the cable motion evolve to its preferred time-asymptotic response. For computational simplicity we only consider a constrained cable vibrating in the crossflow direction. Three cases corresponding to three different cable tensions are considered. The three tensions are chosen to attempt to select, i.e. amplify, vibrations with spanwise wavelengths of $L/d = 6.3, 12.6$, and 25.1. The initial cable crossflow displacement is shown in figure 18. This initial displacement shows a waveform composed of several wavelengths, and the maximum amplitude of the waveform is relatively small.

The three simulations have identical cable and flow initial conditions – the only difference is the cable tension. The simulations for the three tension cases are run for more than 20 shedding cycles. The simulation results for the first 120 time units (approximately 20 shedding cycles) are shown in figure 19. Again, we plot the cable crossflow displacement y/d, versus time tU/d, and position along cable z/d. The lowest tension case, plot (a), shows a standing wave response with a spanwise wavelength of $L/d = 6.3$ emerging after about 15 shedding cycles ($tU/d = 260$). The higher tension case, plot (b), shows a standing wave response emerging after 5 shedding cycles ($tU/d = 210$), but this soon turns into a travelling wave response ($tU/d = 240$) which is then maintained, this time with a spanwise wavelength of $L/d = 12.6$. In the highest tension case, plot (c), the standing wave response emerges very quickly and is sustained for about 10 shedding cycles until $tU/d = 250$, but then it turns into a travelling wave response in this case with a spanwise wavelength

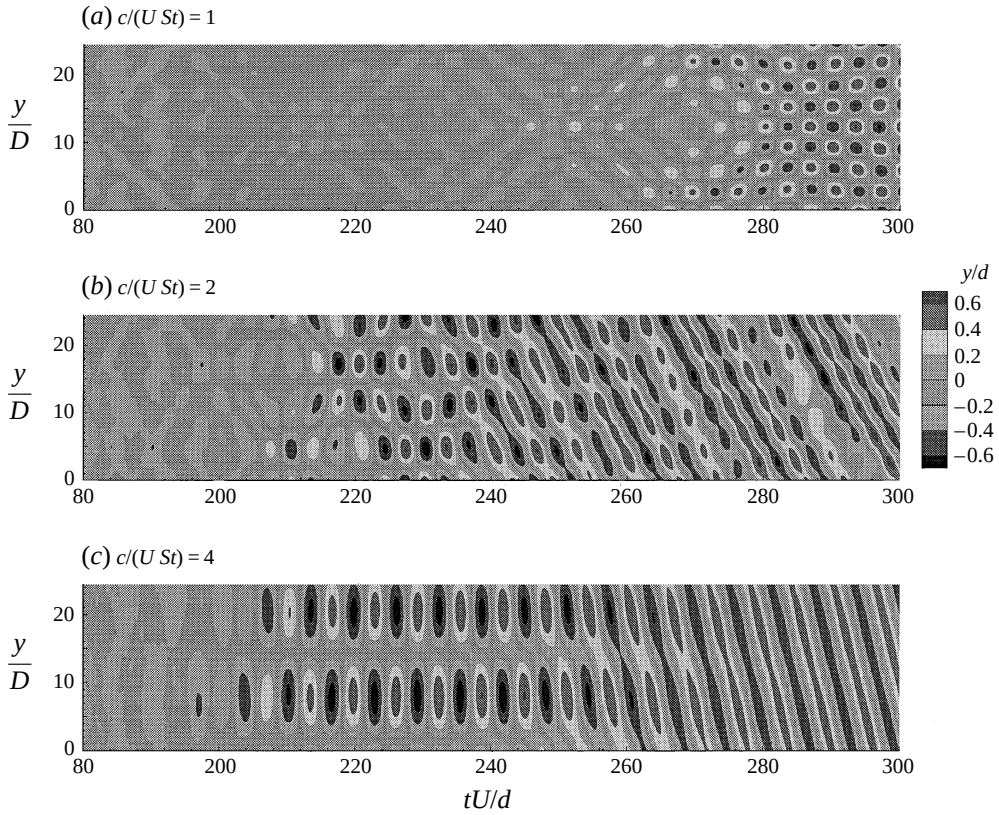

FIGURE 19. Cable crossflow displacement response to random initial conditions. $Re = 100$.

of $L/d = 25.1$. In every case, the maximum amplitude of crossflow displacement is approximately $y/d = 0.7$.

In the lowest tension case, why do we observe an eventual standing wave response, while in the two higher tension cases we observe eventual travelling wave responses? Recall that, as seen in §4.1, the $L/d = 6.3$ vibration wavelength travelling wave response is unstable due to the high angle of oblique shedding, and breaks down to a standing wave response. Consequently, it is not surprising that in this wavelength case we observe the evolution of a standing wave response which persists indefinitely.

4.5. *Fluid/cable energy transfer*

The instantaneous power developed by the lift force F_l acting on the cable which moves at a velocity $\partial y/\partial t$ is given by $W_l = F_l \partial y/\partial t$. Similarly for the drag force, $W_d = F_d \partial x/\partial t$. We compute the power produced by the lift force and drag force for the constrained standing and travelling wave as well as the unconstrained travelling wave. The results are plotted in figures 20 and 21. Of course, for the constrained cable cases, we only compute the power due to the lift force. Positive power means that energy is being transferred from the fluid to the cable. Looking at the standing wave power plot (figure 20*a*), we note several features. First, when the cable velocity is zero, no power is developed – therefore at the cable nodes, and when the standing wave is at maximum amplitude, the instantaneous power is zero. As the cable moves from

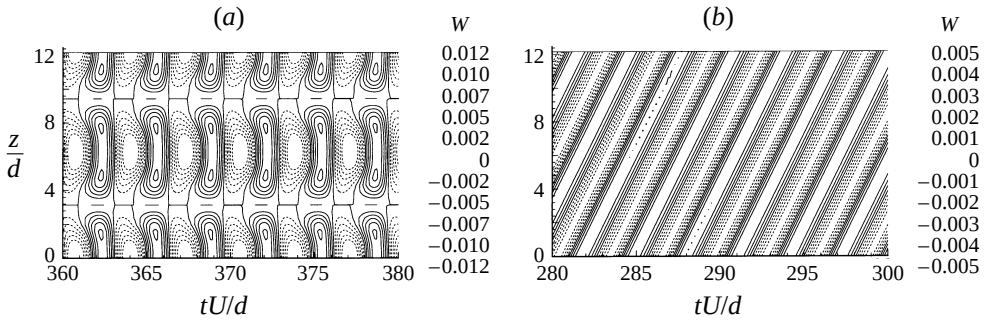

FIGURE 20. Power produced by lift force for standing wave (*a*) and travelling wave (*b*) constrained flow-induced vibrations, $Re = 100$.

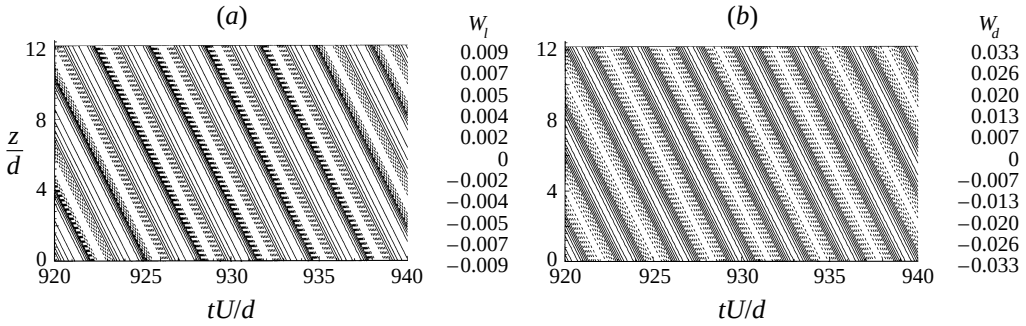

FIGURE 21. Power produced by lift force (*a*) and drag force (*b*) for unconstrained travelling wave flow-induced vibrations, $Re = 100$.

the instant of maximum amplitude, the instantaneous power is negative, indicating that the cable is transferring energy to the fluid. Then the fluid transfers energy back to the cable as it returns to the position of maximum amplitude. For a time-periodic response, the net power exchange over one cycle is zero; otherwise the cable would be in a different state after one period.

As expected, the constrained travelling wave power response in figure 20(*b*) shows the instantaneous power following the same travelling wave pattern as the motion and forces. The magnitude of the power is less than half the peak power measured for the standing wave case. This is due to both the lower magnitude of the lift forces and the lower cable velocity (the velocity is proportional to amplitude) in the travelling wave case.

In the unconstrained travelling wave case we separately compute the power due to the lift force W_l and the drag force W_d. The peak power due to the drag force is more than triple the peak power due to the lift force, and the lift power cycle lags the drag power cycle by approximately 90°.

Is there any pattern of energy transfer in either space or time? Because the travelling wave responses are very close to single-frequency sinusoidal in both space and time, both space and time averages, $E(t) = (1/L)\int_0^L W\,\mathrm{d}z$ and $E(z) = (1/T)\int_0^T W\,\mathrm{d}t$, integrated over one wavelength or period, are practically zero. However, in the case of the standing wave, we get important information from both these quantities. Figure 22 shows $E(z)$, the time average of the power plot in figure 20(*a*). Over one shedding cycle, energy is transferred from the fluid to the cable near the nodes of

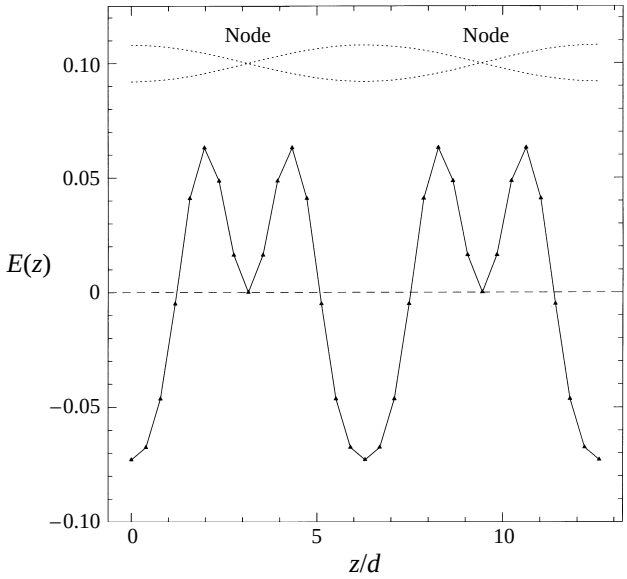

FIGURE 22. Time average of $L/d = 12.6$ standing wave cable power versus span, $Re = 100$.

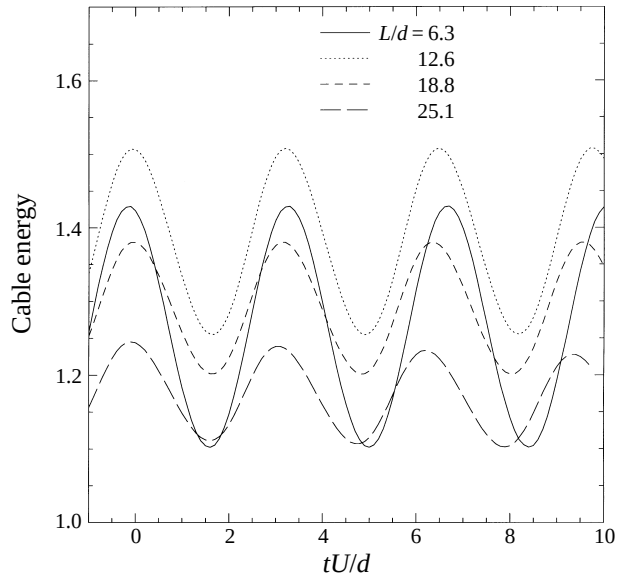

FIGURE 23. Standing wave cable energy versus time for different vibration wavelengths, $Re = 100$.

the standing wave (recall that at the node we get zero power), and from the cable to the fluid at the anti-nodes of the standing wave. This is a somewhat expected result, because the small motion of the cable near the nodes is being forced by the fluid, while the large motion of the cable at the anti-nodes is being damped by the fluid.

The instantaneous cable energy is given by $e(t) = (1/L)\int_0^L (y_t^2 + c^2 y_z^2 + \omega_n^2 y^2)\mathrm{d}z$. This is computed for the constrained standing wave and travelling wave cases. Again, when the cable motion is purely harmonic, this energy will be constant in time. Consequently, for the travelling wave cases, we get $e(t) = \text{const}$. On the other hand,

for the standing wave we get an oscillating cable energy time history. These are shown for the four vibration wavelengths in figure 23. As the vibration wavelength increases, both the mean cable energy and amplitude of cable energy decrease, with the exception of $L/d = 6.3$. The difference between maximum and minimum cable energy decreases with increasing vibration wavelength. This energy difference reflects the amount of energy transferred between the cable and fluid during each vibration cycle.

This oscillation of standing wave cable energy in time and average power versus span, compared to being constant and zero respectively in the case of the travelling wave, is a possible explanation of the observation that the travelling wave is the preferred flow-induced vibration cable response.

5. Response to sheared inflow

Experimental evidence that sheared inflow can lead to a multi-moded vibration response of the cable which prevents global synchronization has been reported by Vandiver (1991). Other effects of linear shear have been investigated in Kim, Vandiver & Holler (1986), Peltzer (1985) and Venugopal (1996). When the incoming flow is sheared, different sections of the cable experience a different free-stream velocity, and consequently vortices are shed at different frequencies. This mismatch in vortex shedding frequency along the span of the cable disrupts the vortex shedding pattern and may lead to a multi-moded vibration response. We can simulate a sheared inflow in the context of the spanwise-periodic model by specifying a sinusoidal inflow, e.g. $u(-\infty, y, z) = u_0 + \epsilon \cos(2\pi z/L)$. For our simulation we set the inflow velocity to $u(-\infty, y, z) = (3+\cos(2\pi z/L))/4$, i.e. the free stream varies between $u = 1$ and $u = 0.5$, and we get a corresponding range of Reynolds numbers from $Re = 100$ to $Re = 50$. To encourage a greater range of vibration response, we simulated a long section of cable with a periodic length $L/d = 100$. The simulation was run for several hundred time units. The results for the crossflow displacement y/d, lift coefficient C_l, power W, and drag coefficients C_d, versus time tU/d, and position along cable z/d, are shown in figure 24. For this simulation, the lift and drag coefficients are normalized with the *minimum* free-stream velocity of $u = 0.5$, so the force coefficients actually represent the magnitude of the forces.

The cable's crossflow displacement shows a mixed standing wave/travelling wave response forming an overall chevron pattern, similar to what Albarede & Monkewitz (1992) modelled. The maximum amplitude of the response is $y/d = 0.4$. The cable's motion is smaller on average at $z/d = 50$, where the inflow is at a maximum, $u = 1$. The lift coefficient plot shows this chevron pattern even more clearly, but with the largest amplitudes occurring near the spanwise locations of intermediate inflow velocity. The drag force at maximum inflow is approximately three times the drag force at minimum inflow, almost consistent with the square of the twofold increase in inflow velocity.

Instantaneous power is on average positive at maximum inflow and negative at minimum inflow. To examine the average power as a function of spanwise position, we plot $E(z) = (1/T)\int_0^T W \mathrm{d}t$ in figure 25. The spiky nature of this curve is due to the many vibration nodes along the cable, where the instantaneous power is zero. We deduce from this plot that on average, where the inflow velocity is above $u = 0.75$ (between $z/d = 30$ and $z/d = 70$), the fluid is supplying energy to the cable, and where the inflow velocity is below $u = 0.75$, the cable is supplying energy to the fluid. Since the computed cable energy is approximately constant in time, this could

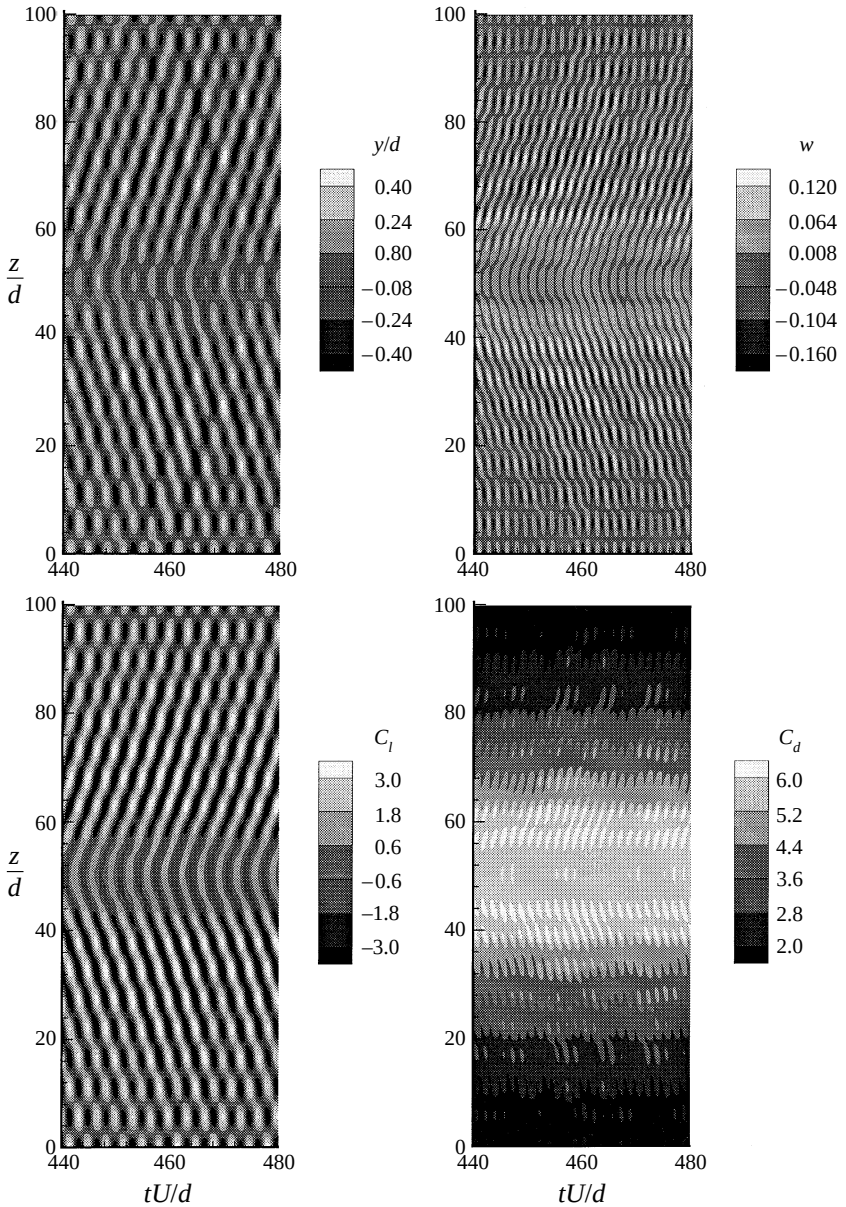

FIGURE 24. Cable crossflow displacement, power, lift coefficient and drag coefficient versus time and distance along cable for sheared inflow cable response L/d=100. Note that the lift and drag coefficients are normalized with the minimum free-stream velocity.

alternatively be viewed as a transfer of energy along the cable from the location of maximum inflow towards the location of minimum inflow. This transfer is reflected in the chevron patterns seen in the displacement response. Because we are measuring flow-induced vibrations with relatively constant amplitude, the net area under the curve in figure 25 is negligible, i.e. $\int_0^L \int_0^T W \mathrm{d}t\mathrm{d}z \approx 0$. The energy transfer shown in this plot is characteristic of non-lock-in, where power injected at one location and

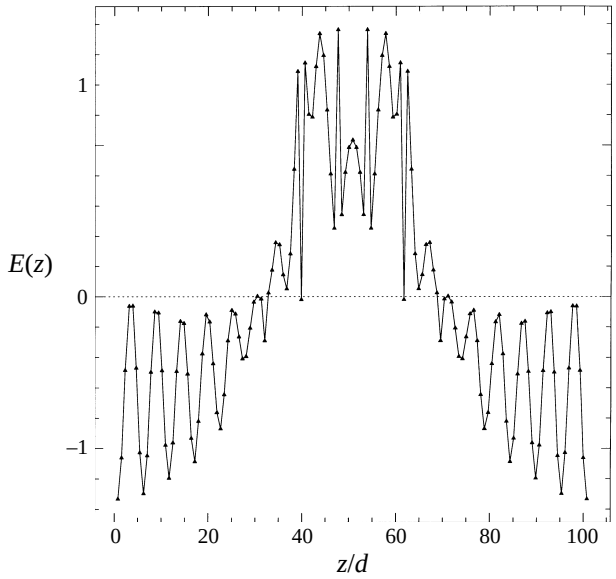

FIGURE 25. Time average of cable power when responding to sheared inflow. Inflow velocity is maximum at z/d=50 and minimum at $z/d = 0$ and $z/d = 100$.

frequency on the cable is dissipated into the fluid at a different position on the cable, which is exposed to a different inflow velocity, as described by Kim *et al.* (1986).

Figure 26 shows an iso-surface of spanwise vorticity from this sheared inflow case. For clarity, we have plotted just one value of negative spanwise vorticity. The figure clearly shows the higher frequency of shedding at the location of maximum inflow $z/d = 50$, and lower frequency of shedding at the location of minimum inflow $z/d = 100$. This difference in shedding frequency along the span causes vortex dislocation (seen in the figure at approximately $z/d = 65$). Vortex dislocation has been observed in experiments by Williamson (1992) and Eisenlohr & Eckelmann (1989) and in numerical simulations with a stationary cylinder at higher Reynolds number by Henderson & Karniadakis (1995).

6. Transitional flow at $Re = 200$

All the $Re = 100$ flow-induced vibration simulations result in time-periodic cable and flow responses after the transients die out. To investigate the effect of higher Reynolds number, we conducted simulations examining the case of unconstrained cable flow-induced vibrations at $Re = 200$ for the $L/d = 12.6$ spanwise wavelength case. This wavelength was chosen for two reasons. First, throughout this study $L/d = 12.6$ is considered the 'base' spanwise wavelength to make comparisons between different simulations easier. Second, the shorter wavelength offers reasonable resolution (mesh spacing in the z-direction is $\Delta z/d = 0.4$), and practical computation times.

We start the $Re = 200$ simulation from the $Re = 100$ unconstrained cable flow-induced vibration simulation results. The simulation runs for more than 100 shedding cycles (> 500 time units) at which point the transients due to the change in Reynolds number die out, and the cable and wake response reach statistical stationarity. The cable displacement, force coefficients, and power for the crossflow and streamwise directions of motion are shown in figure 27. First looking at the crossflow cable

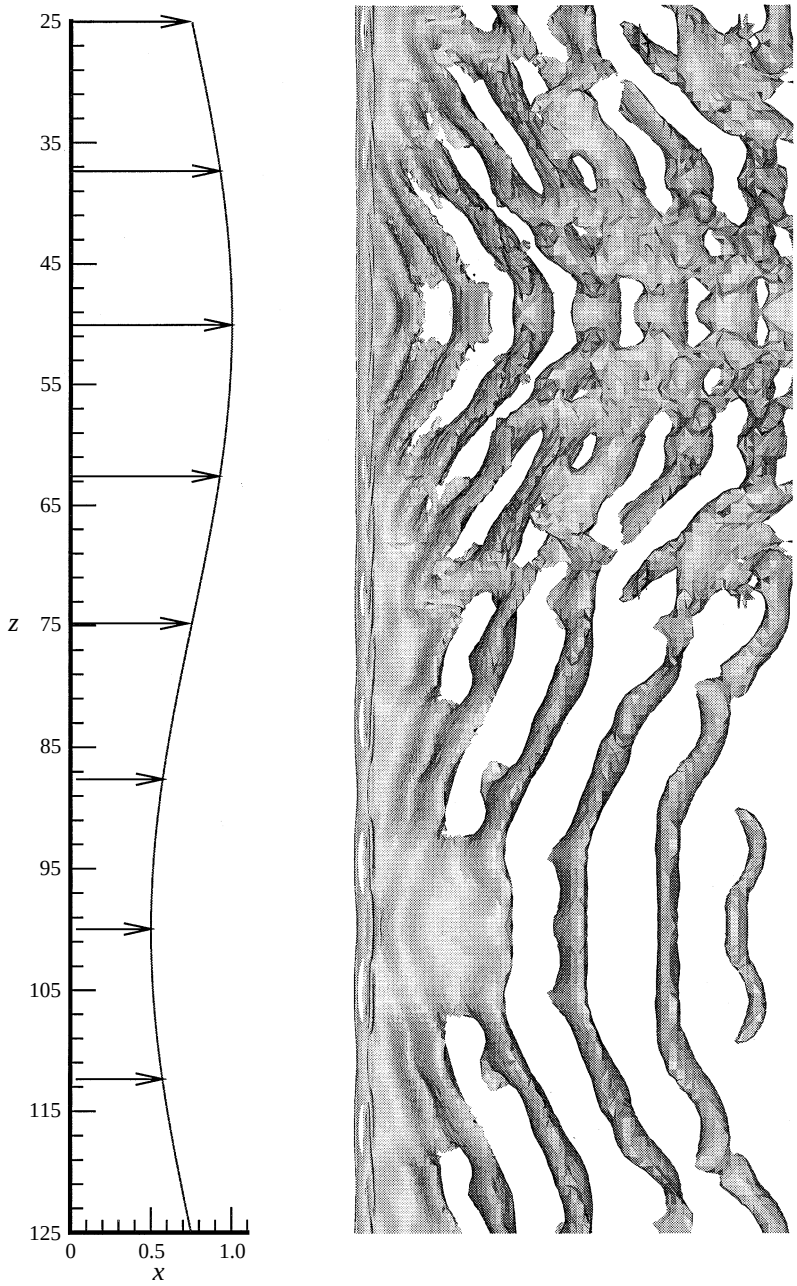

FIGURE 26. Isosurface of spanwise vorticity for sheared inflow cable wake, showing sheared inflow profile varying between $u = 0.5$ and $u = 1$. (Only part of the cable is shown.)

displacement, we see a peak-to-peak amplitude of nearly two cable diameters, close to that observed in experiments shown in figure 1. The range of lift coefficients is nearly four times that measured in the $Re = 100$ unconstrained travelling wave case. The power produced by the lift force is more than double that at $Re = 100$. The peak-to-peak amplitude of cable motion in the streamwise case is approximately 0.7 diameters, compared to less than 0.2 diameters at $Re = 100$. The mean streamwise

Quantity	$Re = 100$	$Re = 200$
std y/d	0.47	0.46
max y/d	0.67	1.05
std C_l	0.22	0.76
max C_l	0.36	1.59
$\bar{x}/d$	45.52	45.13
std x/d	0.06	0.15
$\bar{C}_d$	2.01	1.99
std C_d	0.11	0.65
max C_d	2.16	3.60

TABLE 7. Summary of motion and force results for flow-induced vibrations versus Reynolds numbers $Re = 100$ and $Re = 200$ for L/d=12.6 wavelength cable (std denotes standard deviation and bar describes time-averaged quantities).

cable displacement and mean drag coefficient are about the same in both cases; however, the peak drag force is more than 50% higher at $Re = 200$. Again, we see greater power transfer between cable and fluid due to the drag force rather than the lift force.

Table 7 compares the cable dynamics for the $Re = 100$ and $Re = 200$ flow-induced vibration cases: all the parameters are the same except for the Reynolds number (i.e. the same cable tension and spanwise wavelength). Since the $Re = 200$ response was not time periodic, we also list the standard deviation of the cable motion and forces to provide a better comparison with the $Re = 100$ results: std y/d refers to the standard deviation (about the mean, in the case of x and C_d) of the cable's crossflow amplitude, and max y/d refers to the maximum measured crossflow amplitude. It is best to compare standard deviations, since these will be insensitive to random peaks in motion and forces. Interestingly, we see that the standard deviation of the crossflow displacement is approximately the same for the two Reynolds numbers, despite larger maximum values for $Re = 200$. The standard deviation of the streamwise motion is 2.5 times bigger at $Re = 200$, but the mean drag is approximately the same in both cases. The standard deviation of the drag coefficient is approximately six times larger at $Re = 200$, and the maximum drag coefficient is more than 50% larger at $Re = 200$.

The top view and perspective views of equal and opposite levels of spanwise vorticity ($\omega_z = \pm 0.2$) for the the $Re = 200$ flow-induced vibration wake are shown in figure 28. The flow is going from left to right and the cable is located at approximately $x/d = 45$. We see that the wake is significantly more disorganized than the corresponding wakes at $Re = 100$ – compare with the standing wave and travelling wave wakes at $Re = 100$ in figures 9 and 10. This disorganization may be also due to a possible detuning of the wake but simulations at different tensions showed similar patterns suggesting that the flow at this Reynolds number is indeed in a transitional state (Evangelinos & Karniadakis 1996). It is more difficult to describe the pattern of spanwise vorticity in this case – in fact we see features that resemble both the standing wave and travelling wave wakes at $Re = 100$. To continue the comparison with the $Re = 100$ case, we plot a top view of equal and opposite signs of the three vorticity components in figure 29. We see that the streamwise and normal vorticity components are significantly larger that the spanwise vorticity component. In these plots, contour levels of $\omega = \pm 1$ were chosen for clarity, whereas the corresponding plots at $Re = 100$ (figures 14) were plotted with contour levels of $\omega = \pm 0.2$.

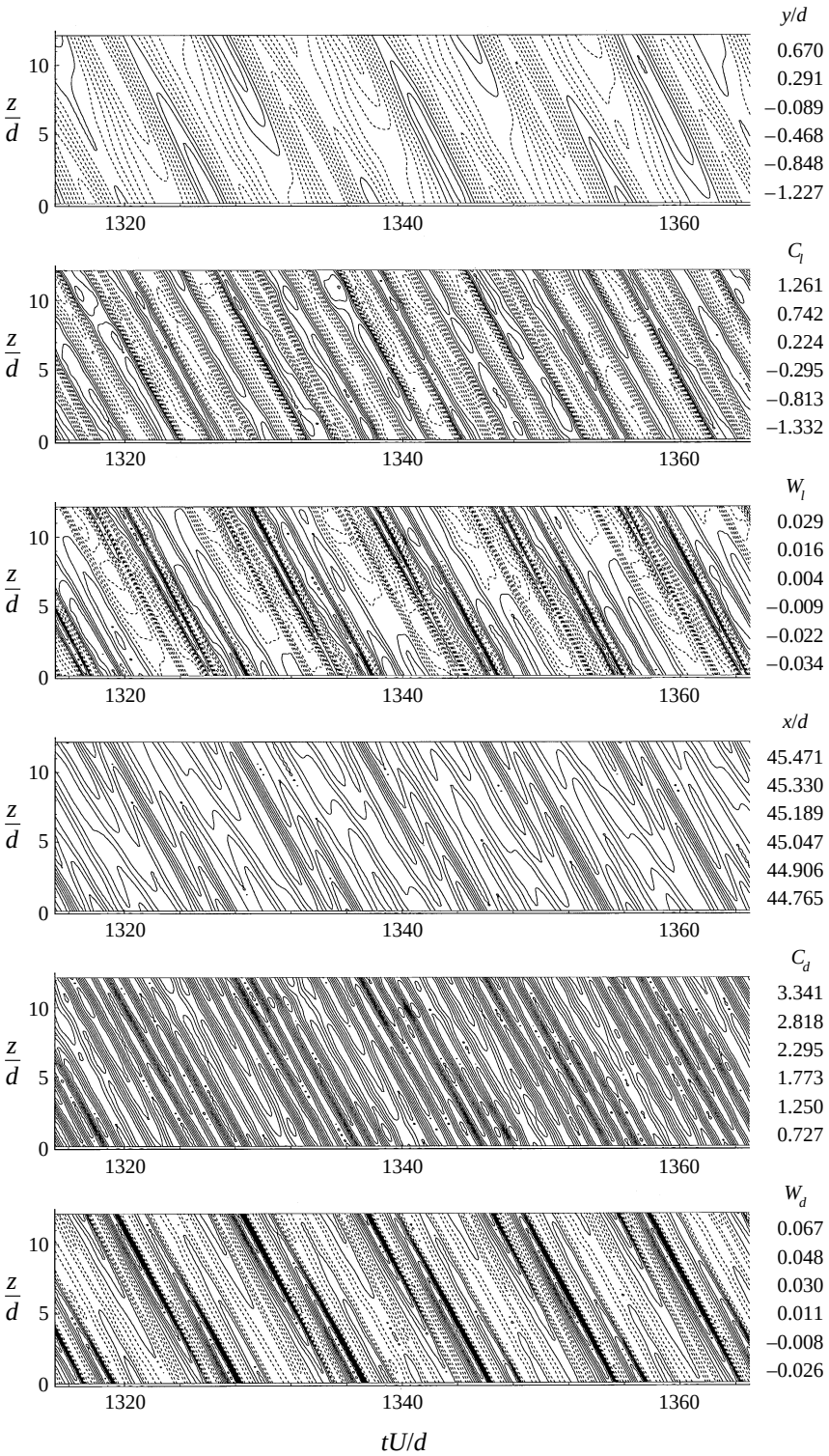

FIGURE 27. Cable displacements, force coefficients and power versus time and distance along cable for $Re = 200$ flow-induced vibration response, $L/d = 12.6$.

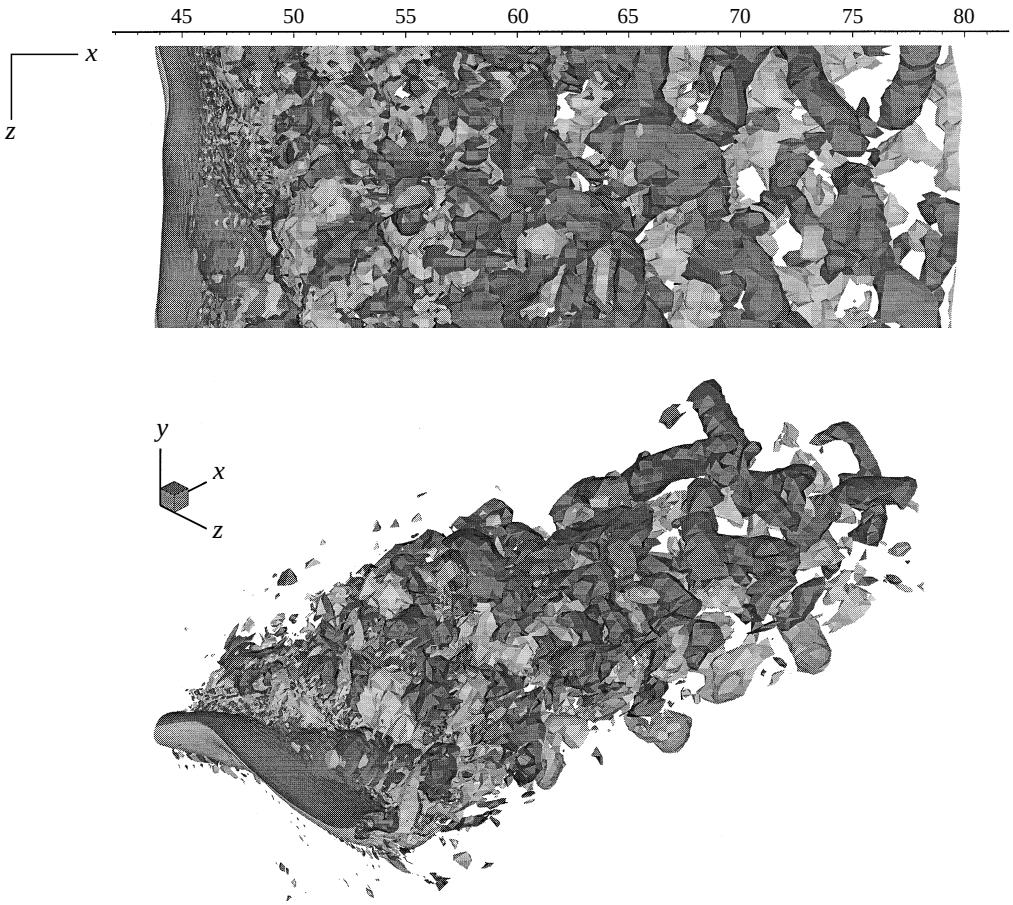

FIGURE 28. Top and perspective views of spanwise vorticity for $Re = 200$ flow-induced vibration response. The two shades are equal and opposite magnitude of spanwise velocity, contour levels $\omega_z = \pm 0.2$, $Re = 200$.

7. Summary and discussion

This paper presents a series of simulations of flow-induced vibrations of a flexible cable at $Re = 100$ and $Re = 200$. The cable vibration wavelength varied from $L/d = 6.3$ to 201.1. Most of the cases presented resulted in a lock-in response, where the cable is vibrating primarily with a single frequency and wavelength. This lock-in response can have the form of a standing wave or travelling wave cable vibration. For the streamwise-constrained cable, both these modes were sustained over several shedding periods. However, the travelling wave cable response prevailed for longer times. For the unconstrained cable, the travelling wave was the only time-periodic response observed. The only case where the cable persisted with a standing wave response was that of a small vibration wavelength ($L/d = 6.3$) streamwise-constrained cable. In general, the travelling wave was the preferred response, clearly visible at $Re = 100$, and still apparent at $Re = 200$. With the absence of any cable end supports, i.e. the assumption of spanwise periodicity, the preference of the travelling wave response can be possibly explained by considering the power cycle throughout one shedding period.

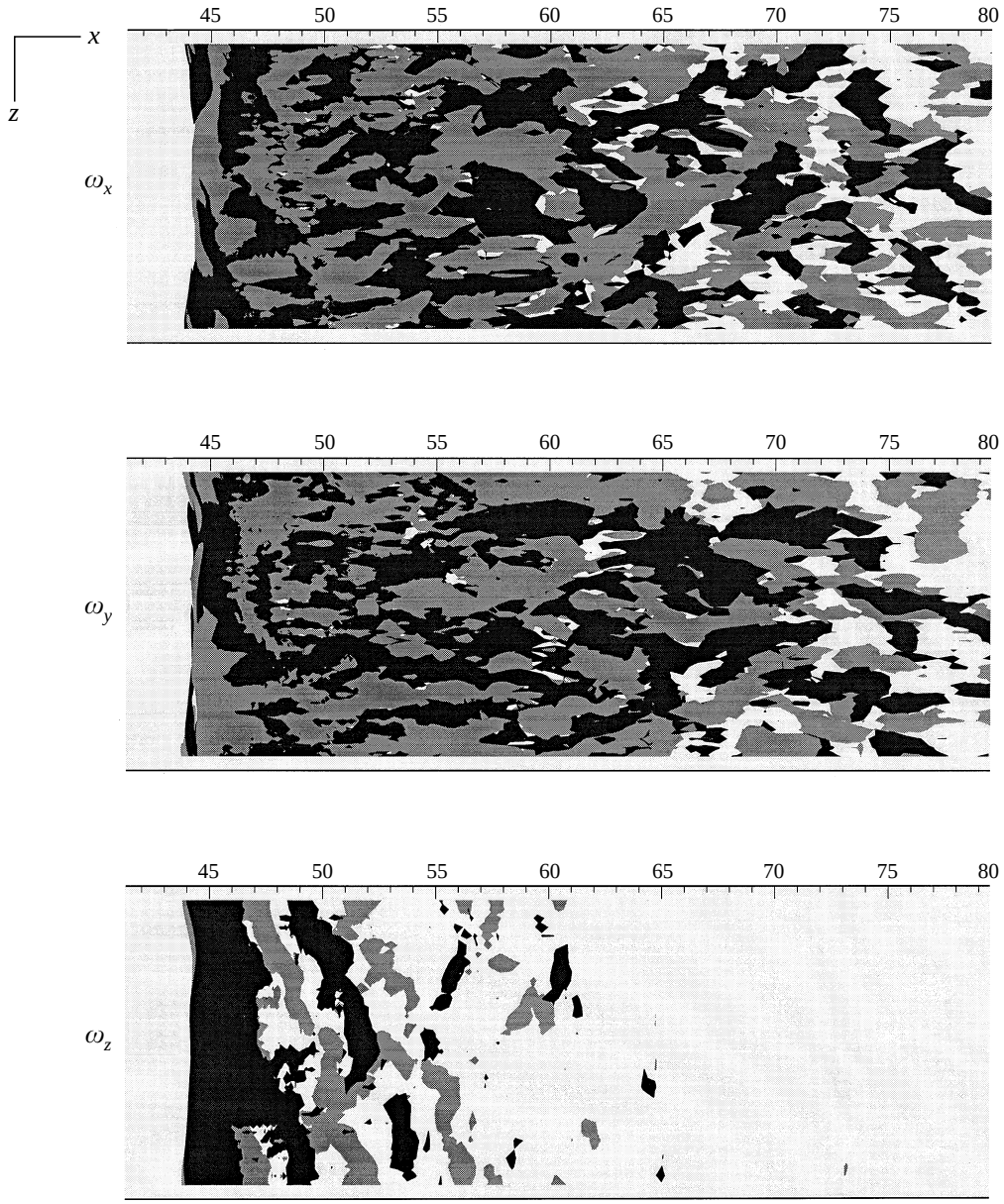

FIGURE 29. Top view of three vorticity components for wake behind cable flow-induced vibrations, $Re = 200$. Contour levels $\omega = \pm 1.0$.

The maximum amplitude of the cable vibration at $Re = 200$ was approximately one cable diameter, in agreement with the experimental data of figure 1. At $Re = 100$ the maximum amplitude of the crossflow vibration is approximately 0.7 diameters, slightly above the amplitude of two-dimensional free vibrations at the same Reynolds number. The three-dimensional simulations showed a greater Reynolds number dependence than the two-dimensional simulations.

There was a sharp contrast between the wakes generated by the standing wave and travelling wave cable responses. In the standing wave case, the two sheets of

spanwise vorticity formed an interwoven pattern, while in the travelling wave case oblique vortex shedding was observed. Furthermore, the maximum lift force for the standing wave was significantly larger than that for the travelling wave.

Both standing wave and travelling wave cable vibration responses are realizable in field and laboratory experiments. Travelling wave responses were observed by Vandiver (1991) and Alexander (1981) for long cables, and Van Atta, Gharib & Hammache (1988) and Van Atta, Gharib (1987) for shorter cables with soft end supports. For cables with non-negligible structural damping, Vandiver (1991) suggests a criterion according to which a travelling wave dominates when the product of the mode number and the modal damping ratio exceeds 2. The effect of the end support has also been documented in the work of Van Atta *et al.* (1988) for a vibrating string using smoke wire visualization. The flow structure shown in the photographs obtained was quite complicated, with the larger structures formed behind the nodes similarly to what has been observed in our simulations. In the photograph in figure 3 of Van Atta *et al.* (1988) owing to the soft support on the right end (M. Gharib, private communication) travelling waves were produced which caused oblique shedding similar to what has been observed in the current simulations.

In this work, we have considered primarily lock-in states; no attempt was made to determine the boundaries of the lock-in regions for freely moving cables. It was demonstrated in the work of Nuzzi, Magress & Rockwell (1992) that even a small variation in the diameter of an oscillating cylinder can change the lock-in region creating subharmonic responses at the lower end of the lock-in boundary. The differences between the lock-in regions of standing versus travelling wave responses, i.e. which one is broader, is also not known. These issues as well as multi-moded responses and higher Reynolds number effects for cables and beams are currently under investigation.

We would like to dedicate this paper to the memory of Dr Owen Griffin with whom we had very fruitful discussions over the years on the subject of fluid/structure interactions. This work was supported by the Office of Naval Research and partially by the National Science Foundation. We would like to thank Dr Tom Swean at ONR who has suggested and has supervised the work. We are very grateful to Professor G. S. Triantafyllou of CCNY, Professor M. Gharib of Caltech, and Professor M. S. Triantafyllou of MIT for discussions regarding this work. Earlier computations were performed on the Intel-Paragons at the San Diego Supercomputing Center and the Caltech Concurrent Supercomputing Facility. Later computations were performed on the IBM-SP2s at the Cornell Theory Center and the Center for Fluid Mechanics at Brown University, which is supported by an NSF grant, an IBM SUR grant, and a grant from Texas Instruments, Inc.

REFERENCES

Albarede, P. & Monkewitz, P. A. 1992 A model for the formation of oblique shedding patterns and chevrons in cylinder wakes. *Phys. Fluids* A **4**, 744.

Alexander, C. M. 1981 The complex vibrations and implied drag of a long oceanographic wire in crossflow. *Ocean Engng* **8**, 379–406.

Barkley, D. & Henderson, R. D. 1996 Three-dimensional Floquet stability analysis of the wake of a circular cylinder. *J. Fluid Mech.* **322**, 215–241.

Bearman, P. W. 1984 Vortex shedding from oscillating bluff bodies. *Ann. Rev. Fluid Mech.* **16**, 125–177.

Blackburn, H. M. & Karniadakis, G. E. 1993 Two- and three-dimensional simulations of vortex-

induced vibration of a circular cylinder. *Proc. 3rd Intl Offshore and Polar Engng Conf., Singapore*, vol. 3, pp. 715–720.

Blevins, R. D. 1977 *Flow Induced Vibrations*. Krieger, Florida.

Brika, D. & Laneville, A. 1993 Vortex-induced vibrations of a long flexible circular cylinder. *J. Fluid Mech.* **250**, 481–508.

Brown, G. L., Karniadakis, G. E. & Young, J. 1993 The turbulent near wake of a half-cylinder at low Reynolds number. *Bull. Am. Phys. Soc.* **38**, 2313.

Carrier, G. F. 1945 On the non-linear vibration problem of the elastic string. *Q. J. Appl. Maths* **3**, 157–165.

Chung, T. Y. 1989 Vortex-induced vibration of flexible cylinders having different mass ratios. *Rep.* UCE 440-1283ED, Korea Research Institute of Ships and Ocean Engineering.

Crawford, C. H., Evangelinos, C., Newman, D. J. & Karniadakis, G. E. 1996 Parallel benchmarks of turbulence in complex geometries. *Computers Fluids* **25**, 677.

Dimas, A. A. & Triantafyllou, G. S. 1994 Nonlinear interaction of shear flow with a free surface. *J. Fluid Mech.* **260**, 211–246.

Eisenlohr, H. & Eckelmann, H. 1989 Vortex splitting and its consequences in the vortex street wake of cylinders at low Reynolds numbers. *Phys. Fluids* A **1**, 189–192.

Evangelinos, C. & Karniadakis, G. E. 1996 Transition in the wake of flexible beams and cables. *Bull. Am. Phys. Soc.* **41**, 1714.

Griffin, O. M. 1992 Vortex-induced vibrations of marine structures in uniform and sheared currents. *NSF workshop on Riser Dynamics, University of Michigan.*

Griffin O. M. & Koopmann G. H. 1977 The vortex-excited lift and reaction forces on resonantly vibrating cylinders. *J. Sound Vib.* **54**, 435–448.

Griffin, O. M., Vandiver, J. K., Skop, R. A. & Meggitt, D. J. 1982 The strumming vibrations of marine cables. *Ocean Sci. Engng* **7**, 461–498.

Griffin O. M., Skop, R. A. & Koopmann, G. H. 1973 The vortex-excited resonant vibrations of circular cylinders. *J. Sound Vib.* **31**, 235–249.

Hammache, M. & Gharib, M. 1991 An experimental study of the parallel and oblique vortex shedding from circular cylinder. *J. Fluid Mech.* **232**, 567–590.

Hartlen, R. T. & Curie, I. G. 1970 Lift Oscillation model for vortex-induced vibration. *J. Engng Mech. Div., ASCE* **96**, 577–591.

Henderson, R. D. & Karniadakis, G. E. 1995 Unstructured spectral element methods for simulation of turbulent flows. *J. Comput. Phys.* **122**, 191–217.

Hover, F. S., Grosenbaugh, M. A. & Triantafyllou, M. S. 1994 Calculation of dynamic motions and tensions in towed underwater cables. *IEEE J. Ocean Engng* **19**, 449–457.

Irvine, H. M. & Caughey, T. K. 1974 The linear theory of free vibrations of a suspended cable. *Proc. R. Soc. Lond.* A **341**, 299–315.

Karniadakis, G. E., Israeli, M. & Orszag, S. A. 1991 High-order splitting methods for incompressible Navier–Stokes equations. *J. Comput. Phys.* **97**, 414–443.

Karniadakis, G. E. & Triantafyllou, G. S. 1992 Three-dimensional dynamics and transition to turbulence in the wake of bluff objects. *J. Fluid Mech.* **238**, 1–30.

Kim, Y. H., Vandiver, J. K. & Holler, R. 1986 Vortex-induced vibration and drag coefficients of long cables subjected to shear flow. *J. Energy Resources Technol.* **108**, 584–592.

Lighthill, J. 1986 Fundamentals concerning wave loading on offshore structures. *J. Fluid Mech.* **173**, 667–681.

Naudascher, E. & Rockwell, D. 1993 *Flow-Induced Vibrations. An Engineering Guide*. A.A. Balkema, Rotterdam.

Nuzzi, F., Magness, C. & Rockwell, D. 1992 Three-dimensional vortex formation from an oscillating, nonuniform cylinder. *J. Fluid Mech.* **238**, 31–54.

Newman, D. J. 1996 A computational study of fluid/structure interactions: flow-induced vibrations of a flexible cable. PhD thesis, Princeton University.

Newman, D. J. & Karniadakis, G. E. 1995 Direct numerical simulations of flow over a flexible cable. *Proc. Sixth Intl Conf. on Flow-Induced Vibration* (ed. P. W. Bearman), pp. 193–203. Balkema, Rotterdam.

Ongoren, A. & Rockwell, D. 1988 Flow structure from an oscillating cylinder, Part 1: Mechanisms of phase shift and recovery in the near wake. *J. Fluid Mech.* **191**, 197–223.

Parkinson, G. 1989 Phenomena and modelling of flow-induced vibrations of bluff bodies. *Proc. Aero. Sci.* **26**, 169–224.

Peltzer, R. D. & Rooney, D. M. 1985 Near wake properties of a strumming cable: An experimental study. *Trans ASME: J. Fluids Engng* **107**, 86–91.

Ramberg, S. E. & Griffin, O. M. 1976 The effects of vortex coherence, spacing, and circulation on the flow-induced forces on vibrating cables and bluff structures. *Naval Research Laboratory Rep.* 7945.

Saffman, P. G. & Schatzman, J. C. 1982 Stability of a vortex street of finite vortices. *J. Fluid Mech.* **117**, 171–185.

Sarpkaya, T. 1977 Transverse Oscillations of a circular cylinder in uniform flow, Part I. *Naval Postgraduate School Rep.* NPS-69SL77071.

Sarpkaya, T. 1979 Vortex-induced oscillations: A selective review. *Trans. ASME: J. Appl. Mech.* **46**, 241–258.

Staubli, T. 1983 Calculation of the vibration of an elastically mounted cylinder using experimental data from forced oscillation. *Trans. ASME: J. Fluids Engng* **105**, 225–229.

Taylor, G. I. 1928 The forces on a body placed in a curved or converging stream of fluid. *Proc. R. Soc. Lond.* A **120**, 260–283.

Triantafyllou, M. S. 1985 The dynamics of translating cables. *J. Sound Vib.* **103**, 171–182.

Triantafyllou, M. S. 1994 Cable mechanics for moored floating systems. *Proc. BOSS'94, Behaviour of Offshore Structures* (ed. C. Chryssostomidis, M. S. Triantafyllou, A. J. Whittle, & M. S. Hoo Fatt), vol. 2, pp. 57–78. Boston.

Triantafyllou, M. S., Gopalkrishnan, R. & Grosenbaugh, M. A. 1994 Vortex-induced vibrations in a sheared flow: A new predictive method. *Proc. Intl Conf. on Hydroelasticity in Marine Technology* (ed. O. Faltinsen, C. M. Larsen, T. Moan, K. Holden & N. Spidsoe), pp. 31–37. Trondheim, Norway.

Triantafyllou, M. S. & Howell, C. T. 1992 Nonlinear impulsive motions of low-tension cables. *J. Engng Mech.* **118**, 807–830.

Van Atta, C. W. & Gharib, M. 1987 Ordered and chaotic vortex streets behind circular cylinders at low Reynolds numbers. *J. Fluid Mech.* **174**, 113–133.

Van Atta, C. W., Gharib, M. & Hammache, M. 1988 Three-dimensional structure of ordered and chaotic vortex streets behind circular cylinders at low Reynolds numbers. *Fluid Dyn. Res.*, The Japan Society of Fluid Mechanics, pp. 127-132, North-Holland, Amsterdam.

Vandiver, J. K. 1991 Dimensionless parameters important to the prediction of vortex-induced vibrations of long, flexible cylinders in ocean currents. *MIT Sea Grant Rep.* MITSG 91–93.

Vandiver, J. K. & Chung, T. Y. 1987 Hydrodynamic damping on flexible cylinders in sheared flow. *Proc. Offshore Technology Conf.*, OTC 5524. Houston.

Vandiver, J. K. & Li, L. 1994 Cases analysis results for workshop on vortex-induced vibrations of marine risers and cables. Trondheim, Norway, May 1984.

Venugopal, M. 1996 Damping and response prediction of a flexible cylinder in a current. PhD thesis, MIT.

Warburton, T. C. & Karniadakis, G. E. 1996 The wake of oscillating cylinder close to a free-surface. *Bull. Am. Phys. Soc.* **41**, 1732.

Williamson, C. H. K. 1992 The natural and forced formation of spot-like 'vortex dislocations' in the transition of a wake. *J. Fluid Mech.* **243**, 393–441.

Williamson, C. H. K. & Roshko, A. 1988 Vortex formation in the wake of an oscillating cylinder. *J. Fluids Struct.* **2**, 355–381.